

1 This is a non peer-reviewed preprint submitted to EarthArXiv.
2 This manuscript has been submitted to PNAS for peer review
3 Subsequent versions of this manuscript may have slightly different content. We welcome feedback. Please contact Rienk
4 Smittenberg (rienk.smittenberg@geo.su.se) regarding this manuscript's content
5
6

7 **A 18,000 yr record of tropical land temperature, convective** 8 **activity and rainfall seasonality from the maritime continent**

9
10 Rienk H Smittenberg ^{1,*}, Kweku A Yamoah ^{1,2}, Frederik Schenk ^{1,3}, Akkaneewut Chabangborn ^{1,4},
11 Sakonvan Chawchai ^{1,4}, Minna Väiliranta ⁵ and Barbara Wohlfarth ^{1,*}

12 ¹ Department of Geological Sciences and Bolin Centre for Climate Research, Stockholm
13 University, Stockholm, Sweden

14 ² now at School of Geography, University of Birmingham, Birmingham, UK

15 ³ Rossby Centre, Swedish Meteorological and Hydrological Institute, 601 76 Norrköping, Sweden

16 ⁴ now at Department of Geology, Chulalongkorn University, Bangkok 10330, Thailand

17 ⁵ Environmental Change Research Unit, Department of Environmental Sciences, University of
18 Helsinki, Finland

19 *corresponding authors: rienk.smittenberg@geo.su.se ; barbara.wohlfarth@geo.su.se

20
21 **Author Contributions:** BW and RHS designed the study. BW, AC, SC, and KY performed
22 fieldwork and sub-sampled the sediment cores. BW selected samples for ¹⁴C dating and MV
23 performed macrofossil and charcoal analysis. SC performed element analysis. KY performed lipid
24 biomarker and isotope analysis. RHS performed GDGT analysis. FS assisted in GDGT data re-
25 calibration. RHS interpreted the data and wrote the paper with assistance of all authors.

26 **Competing Interest Statement:** There are no competing interests.

27 **Classification:** Physical Sciences; Earth, Atmospheric, and Planetary Sciences

28 **Keywords:** Paleoclimate, Indo-Pacific Warm Pool, Sundaland, Seasonality

29
30 **This PDF file includes:**

31 Main Text
32 Figures 1 to 4
33 Supplementary text with Figures S1-S10
34

35

36 **Abstract**

37 The maritime continent exports an enormous amount of (latent) heat and moisture to the rest of the
38 globe via deep atmospheric convection. How this export has changed through time under evolving
39 boundary conditions, including the inundation of former Sundaland, is critical for the understanding
40 of global climate dynamics. Given its size, relatively few high-resolution and continuous records
41 exist of past hydroclimate, while terrestrial paleotemperature records are still completely absent
42 from the region. In this study we present a 18,000-year multi-proxy record obtained from a lake
43 sediment at the NW corner of former Sundaland. We found that rainfall seasonality was very
44 important over the entire deglacial period, evidenced by biomass burning and C4 vegetation,
45 despite rising atmospheric CO₂ levels and increasing humidity that normally promotes C3
46 rainforests. The strong seasonality was reduced only upon ongoing inundation of Sundaland, with
47 a clear inflection point around the Older Dryas event (13.8 ka BP), indicating a distinct system
48 change. Land temperatures during the last stadial periods were 5°C colder than today's 27°C.
49 Temperatures rose gradually during the early Holocene to reach 29°C between 7-2 ka BP,
50 accompanied by increasing convection, both driven by insolation power during the wet season.
51 Convection decreased with lowering wet-season (autumn) insolation during the Meghalayan
52 period, concurrent with the known increase of ENSO variability and Northern Hemisphere climate
53 cooling and drying. Our results provide further insight in the role of Sundaland - turned maritime
54 continent for the global climate system in response to sea level rise and orbital forcing.

55

56 **Significance Statement**

57 We generated a continuous, 18,000-year land-based paleoclimate record from the northwest
58 corner of former Sundaland in present-day southern Thailand. We found evidence for a strongly
59 seasonal climate for most of the deglacial period, causing biomass burning and suppression of
60 rainforest growth. Terrestrial temperatures were *ca.* 5°C cooler than today during the last cold
61 stadial periods, and *ca.* 2°C warmer between 7000-2000 yr ago, a larger range compared to tropical
62 ocean reconstructions. Comparison of our new and other water isotope records from the region
63 with wettest-season insolation strength, suggests a strong control of the latter on the amount of
64 heat and moisture that gets exported away via deep atmospheric convection, thereby influencing
65 global climate dynamics.

66

67

68 **Main Text**

69

70 **Introduction**

71

72 The maritime continent (MC) forms the central part of the Indo-Pacific Warm Pool (IPWP), defined
73 as the equatorial region with sea surface temperatures (SST) above 28°C. This region is also called
74 the 'steam engine of the world', as it constitutes a critical component of the global climate system
75 by providing large amounts of latent heat to the higher latitudes via deep atmospheric convection,
76 particularly via the monsoon systems (1). The IPWP also forms a key node in the tropical Walker
77 circulation above the Indian and Pacific Ocean, which is modulated by the El Niño-Southern
78 Oscillation (ENSO) (2) and Indian Ocean Dipole (IOD) (3). Changes in rainfall in the MC have large
79 consequences for both society and ecosystems, where drought-induced biomass burning and peat
80 oxidation can induce rapid release of large amounts of carbon to the atmosphere e.g.(4). A major
81 change in the MC over the last glacial-interglacial (G-I) transition was the inundation of formerly
82 exposed Sundaland and the Sahul shelf north of Australia. It has long been recognized that the
83 submergence of this vast tropical landmass must have had substantial consequences for global-

84 scale climate dynamics (3)(5)(6)(7)(8). Palynological data from the former North Sunda and
85 Molengraaff rivers and their deltaic deposits indicate that the region was covered with lowland
86 rainforest that included sedges, reeds, bamboo, palms and ferns, suggesting fairly humid
87 conditions throughout the last glacial maximum (LGM) around Borneo (9, 10). In contrast, other
88 proxy records from the region indicate drier conditions during the LGM (6)(11). Highest ('driest')
89 $\delta^{18}\text{O}$ values are recorded in a Borneo speleothem record at that time (12), and evidence exists for
90 forest contraction and generally drier conditions in both peninsular Malaysia and Palawan during
91 the LGM suggesting the existence of a savannah corridor (13)(14)(15). The somewhat conflicting
92 proxy evidence can be explained by the expanse of former Sundaland which is about the size of
93 the Amazon basin. Another explanation may lie in rainfall seasonality, which can strongly impact
94 proxy records of both vegetation and the recorded water isotope signal. A main problem is,
95 however, that the spatial coverage of high-resolution paleoclimate records from the region remains
96 scant, which is partially explained by the fact that much of Sundaland has disappeared under the
97 waves. Insight into the spatial patterns and mechanisms of the, sometimes rapid, climatic changes
98 that occurred during the G-I transition, as well as over the Holocene, is therefore still limited for this
99 climatically important region. Here, we present a high-resolution and continuous 18,000 year-long
100 multi-proxy record from lake Nong Thale Prong (NTP, $8^{\circ}17'N$, $99^{\circ}37'E$) located in southern
101 Thailand at the northwestern border of former Sundaland (Fig. 1). Lake NTP is a shallow (<7 m
102 water depth), small (~210 m²) karst lake at ~60 m above sea level (16). More details of the lake
103 setting can be found in an earlier publication (17) that focused on the ecological evolution over the
104 last 150 years using ancient DNA and lipid biomarkers. We used the stable carbon isotopic
105 composition of leaf wax-derived long-chain *n*-alkanes ($\delta^{13}\text{C}_{\text{wax}}$) as a proxy for the relative
106 abundance of C3 vs. C4 vegetation, which is influenced by pCO_2 , temperature and seasonality
107 (11)(18). This data set was combined with the stable hydrogen isotope composition of the same
108 leaf wax alkanes ($\delta\text{D}_{\text{wax}}$) and charcoal to gain further information about hydroclimate (19) and
109 seasonality. We also present the first high-resolution land-based temperature record of the IPWP,
110 based on bacterial-derived branched glycerol dialkyl glycerol tetraethers (brGDGTs) (20)(21)(22).
111 The combined proxy records reveal how the aerial exposure and subsequent inundation of
112 Sundaland interacted with orbital variation and other climate forcings to impact the hydroclimate of
113 SE Asia.

114
115

116 Results

117
118

118 *Proxy validation*

119 We performed a present-day proxy evaluation and calibration by comparing proxy data analyzed
120 from the surface sediments with instrumental data for the last century. $\delta\text{D}_{\text{wax}}$ (17) closely follows
121 the annual precipitation amount (Fig. 3a), where a 10‰ decrease in $\delta\text{D}_{\text{wax}}$ corresponds to a 25%
122 reduction in rainfall. This confirms earlier work relating convective activity with both greater rainfall
123 and isotopic fractionation (the 'amount effect', e.g. (23) assuming that $\delta\text{D}_{\text{wax}}$ predominantly reflects
124 $\delta\text{D}_{\text{precip}}$ after biosynthetic fractionation. Previous research has shown that the hydrogen isotopic
125 composition of both terrestrial and aquatic biomarkers generally reflects that of their source water,
126 although with an offset primarily due to biosynthetic fractionation effects (19, 24, 25). In the humid
127 tropics, the fractionation ($\epsilon_{\text{wax/water}}$) was found to be fairly constant at 130‰ (26). Using this
128 fractionation factor, back-calculated δD values for precipitation of the last century ranges between
129 -40‰ and -60‰, reflecting actual measurements for the region (27).

130 Reconstructed mean annual air temperatures (MAAT_{RC}) (Fig 2b) obtained using the relative
131 abundance of microbial-derived branched GDGTs (22)(21), were recalibrated using instrumental
132 temperature data, thus generating a local calibration for this molecular proxy (See Supplementary
133 Information). MAAT_{RC} and $\delta\text{D}_{\text{wax}}$ correlate strongly with each other (Fig 2c), and have the same
134 relation to each other as observed during the seasonal cycle: clear skies during the drier seasons
135 and years with less convective rainfall allow for higher surface temperatures, whereas high clouds

136 associated with deep convection result in a cooling of the surface due to reflection and atmospheric
137 absorption of shortwave radiation (28), an effect that is particularly strong in monsoonal Asia (29).

138

139 *Sedimentology and limnology*

140 The 18,000 year-long lake NTP sequence consist of organic rich gyttja with TOC contents ranging
141 between 10-40% (Fig. S2). TOC contents vary stepwise between 10 and 40% during the deglacial
142 part of the core, high TOC contents between 9.5-4.2 ka BP, turning to somewhat lower and more
143 variable contents over the last few millennia. Besides some variation caused by changes in
144 minerogenic input, we interpret the TOC changes as mainly caused by alternations between
145 meromictic conditions with permanent bottom water anoxia - leading to preservation of organic
146 matter, and monomictic conditions - resulting in greater organic matter oxidation within the
147 sediments. Stratification in tropical lakes is sensitive to small changes in the lake water level
148 between wet and dry seasons, heat budgets and climate (e.g., wind stress), and other limnological
149 or even ecological feedbacks (30). Given this multitude of factors, we do not attempt to interpret
150 the TOC content. Notably, there is no correlation between the variable TOC content and the lipid
151 biomarker proxies presented further below. This indicates that lake stratification and preservation
152 of organic matter did not influence the primary climatic signal of our proxy records.

153 The continuous occurrence of seeds of the aquatic plant taxon *Najas* (Fig. 3f; SI Table 4) and a
154 robust age model (Fig. S1) indicates that the shallow lake never dried out. *Cyperaceae* spp.
155 remains, mostly seeds, also occur continuously throughout the sequence, except for the last few
156 millennia when they are nearly absent.

157 The lower part of the sequence, deposited during Heinrich Stadial 1 (HS1, 18-14.7 ka BP), contains
158 unidentified terrestrial plant remains including woody material, often co-occurring with charred plant
159 remains and macroscopic charcoal; this was also the case for the Younger Dryas period (YD 12.8-
160 11.5 ka BP). Charcoal was most abundant during HS1, then declined towards the end of the
161 deglacial period, with irregular occurrences until the early Holocene around 9 ka BP. Ostracods
162 shells are abundant throughout the HS1, leading to high carbonate contents, and this declines
163 during the Bølling (Bø 14.7-14.0 ka).

164

165 *Temperature reconstruction*

166 MAAT_{RC} (Fig. 3b) stays around 23-24°C during HS1, a 5°C cooling compared to present. This is
167 lower than the most recent estimate for the tropical ocean during the LGM (-4.2 to -3.7°C; (31) but
168 is in line with estimates based on tropical glacier snow line elevations (32). Temperatures rose
169 during the Bø to reach a maximum of 26°C soon after the Older Dryas event (OD 14.0-13.8 ka BP),
170 but declined during the Allerød (Al, 13.8-12.8 ka BP) and again reached stadial values at the end
171 of the YD. With the start of the Holocene temperatures rose steadily to reach 28-29°C between 7-
172 2 ka BP. The last two millennia are characterized by a cooling trend to a present-day MAAT_{RC} of
173 around 27°C.

174

175 *$\delta^{13}\text{C}_{wax}$ as combined proxy for $p\text{CO}_2$, temperature and rainfall seasonality*

176 Stable carbon isotope ($\delta^{13}\text{C}$) values of both of the long-chain *n*-alkanes ($\delta^{13}\text{C}_{wax}$) (Fig. 3c) and the
177 bulk (SI Fig. 2) reflects a change from a landscape dominated by C4 grasses and sedges at the
178 beginning of the record, to a humid tropical ecosystem dominated by ^{13}C -depleted C3 vegetation –
179 likely forest - during the Holocene (*cf.* 33). The $\delta^{13}\text{C}$ record broadly follows the evolution of
180 atmospheric CO_2 (Fig. 3d). This lends support to the hypothesis that low CO_2 concentration favored
181 C4 vegetation during the LGM (34)(35)(18). Our observation compares well to tropical African
182 records (36)(37)(38). Increasing fractionation against ^{13}C at higher $p\text{CO}_2$ levels and greater
183 humidity (39)(40) – regardless of plant type, can explain part of the trend, especially during the
184 Holocene. An exception to the general trend of increasingly more negative $\delta^{13}\text{C}$ from the LGM

185 through the Holocene is a large excursion that starts at 16.0 ka BP, reaching the lowest $\delta^{13}\text{C}$ values
186 at 13.8 ka BP.

187
188

189 *δD_{wax} as proxy for precipitation*

190 To further investigate past precipitation changes, we analyzed δD_{wax} with higher resolution between
191 17-10 ka BP to discern trends during deglaciation (Fig. 3a). δD_{wax} was corrected for the effect of
192 global ice volume (41). A confounding factor in the interpretation of δD_{wax} is the potential effect of
193 changing vegetation and associated change in fractionation (42). For instance, C3 and C4 plant
194 types tend to fractionate differently against deuterium and may moreover respond differently to
195 drought in order to minimize water loss while still allowing gas exchange through the stomata
196 (33)(43). The generally stronger biosynthetic fractionation against deuterium of C3 plants
197 compared to C4 would however lead to an opposite behavior of δD_{wax} as observed: the increase in
198 C4 during the Bølling period is associated with more negative δD_{wax} , not more positive. The same
199 argument can be made from a possible transition from a grassy to more woody vegetation during
200 the G-I transition, which would be expected to lead to less negative δD_{wax} values (42), but again
201 the opposite is observed. From the perspective of vegetation change, our δD_{wax} record might thus
202 even underestimate the original variations in source water δD .

203
204

205 **Discussion**

206 *Deglacial climate evolution*

207 The unusual $\delta^{13}\text{C}$ excursion that starts at 16.0 ka BP suggests a renewed contribution of C4
208 vegetation to the carbon pool in this interval, even though the excursion is coincident with continued
209 warming and its onset correlates with a change in the rate of increase in atmospheric $p\text{CO}_2$ (Fig.
210 3). The behavior of the $\delta^{13}\text{C}$ record indicates that the tropical lowland ecosystem of Sundaland
211 represented an ecotone inhabiting the C3/C4 crossover line during the deglacial period. The
212 ecosystem was thus sensitive to the antagonistic effects of rising $p\text{CO}_2$ and rising temperature on
213 C3 versus C4 plants, where higher temperatures but lower $p\text{CO}_2$ favor C4 plants. However, a third
214 important climatic factor also favors non-perennial C4 vegetation: rainfall seasonality (11).
215 Seasonal dryness was likely promoted by the presence of Sundaland, which only became fully
216 inundated around 11 ka BP during Meltwater Pulse 1b (44). This large landmass prevented the dry
217 northern winds of the Asian winter monsoon from picking up moisture over the Sunda Sea as they
218 do today. This effect was probably promoted by orbital forcing: insolation during NH winter declined
219 while summer insolation increased over the deglacial period, favoring the strength of both the winter
220 and summer monsoon. Strong seasonality promotes biomass production during the wet season,
221 which then serves as fuel for biomass burning during a longer dry season (45). This severely limits
222 the establishment of perennial C3 forests that would otherwise outcompete non-perennial C4
223 vegetation as atmospheric CO_2 levels rose. The charcoal record (Fig. 3f, SI Table 4) provides
224 evidence that fires were a persistent feature during the entire deglacial period, especially during
225 HS1. We therefore conclude that the return towards a larger contribution of C4 vegetation after 16
226 ka BP arose from a combination of both rising temperatures and greater seasonality in rainfall
227 patterns, temporarily offsetting the C3-promoting effect of increasing $p\text{CO}_2$. The return of C3
228 vegetation after 13.8 ka BP, despite the stagnation of CO_2 rise until 12 ka BP, indicates that the
229 region started to have year-round precipitation, reducing seasonal drying and fire. The general
230 trend in $\delta^{13}\text{C}$ observed at NTP also is evident in the lower resolution IPWP record from Lake Towuti
231 on Sulawesi (46)(Fig. S3), supporting the interpretation of the combined influence of $p\text{CO}_2$ and
232 rainfall seasonality over the entire IPWP over G-I timescales.

233

234 Starting at 18 ka BP, the δD_{wax} record increases to reach highest (least negative) values around 16
235 ka BP (Fig. 3), indicating that the driest conditions with the weakest convection and greatest
236 evapotranspiration (47) occurred during HS1. This is followed by a rapid decrease during the Bø,
237 and, similar to the MAAT_{RC} and $\delta^{13}\text{C}$ records, a sharp reversal at the start of the AI. δD_{wax} , MAAT_{RC}

238 and $\delta^{13}\text{C}$ track each other until the YD, with lower (higher) $\delta\text{D}_{\text{wax}}$ and higher (lower) MAAT_{RC} -
239 suggesting warmer and wetter (colder and drier) conditions – consistent with inferences from the
240 $\delta^{13}\text{C}$ record of patterns of change in C4 vegetation. The combined records suggest that the period
241 of high rainfall seasonality also had wetter wet seasons. Yet despite increased humidity and warmer
242 conditions during the wet season, C4 grasses and sedges were not completely replaced by C3
243 plants.

244 We suggest that the steep change in $\delta\text{D}_{\text{wax}}$ between 16 and 14 ka BP was driven by an increase in
245 the convective strength over Sundaland with rising temperatures during the Bø. Large-scale
246 convective activity and rainfall amount are the dominant factors that influence water isotope values
247 in tropical SE Asia, in addition to changes in moisture source region (27). Today, during NH summer
248 (JJA), most moisture in southern Thailand is derived from the Indian Ocean, but during the wettest
249 autumn season (SON) there is also a contribution from the South China Sea. In the past, however,
250 moisture derived from evapotranspiration over Sundaland likely also contributed to the isotopic
251 signature. Moreover, longer air mass trajectories over land would have caused a larger rainout
252 effect, leading to lower water isotope values similar to those of present-day mainland SE Asia (27).
253 The lower values might have been exacerbated by the seasonality of rainfall, because the final
254 isotopic signal of water available for plant growth is biased towards that of the wet season (with
255 lowest $\delta\text{D}_{\text{precip}}$) because of its larger contribution to the weighted annual mean (see supplementary
256 information).

257
258 The rapid sea level rise during MWP1a changed the hydrologic gradient and reduced the flow of
259 Sundaland river systems. Together with monsoon intensification this most likely transformed the
260 entire Sundaland region into a vast expanse of tropical wetlands (1) with abundant moisture and
261 isotope recycling comparable to the present-day Amazon basin. The parallel reversal of $\delta\text{D}_{\text{wax}}$, $\delta^{13}\text{C}$
262 and MAAT_{RC} around 13.8 ka BP, coincident with the OD event (Fig. 3), indicates a system change
263 towards decreasing rainfall seasonality and a more marine climate. Higher year-round moisture
264 availability would result in a greater contribution of less-depleted $\delta\text{D}_{\text{prec}}$ during the cooler winter
265 monsoon months, thereby raising annual mean δD . Lowering of MAAT can occur because of an
266 increase in latent heat production and hence evaporative cooling throughout the year, at the
267 expense of sensible heat. It is also possible that the cold winter monsoon had already started to
268 strengthen during the AI period in response to a southward movement of the mean position of the
269 intertropical convergence zone (ITCZ) caused by NH cooling, something that continued until the
270 end of the YD (~11.5 ka BP). The hypothesis of a southward ITCZ is supported by the coherent
271 patterns in the variability of $\delta\text{D}_{\text{wax}}$ during the YD and the Greenland ice core $\delta^{18}\text{O}$ record, with shifts
272 in the mean position of the ITCZ in response to latitudinal temperature gradients (48). After the YD,
273 however, $\delta\text{D}_{\text{wax}}$ continues to increase until 11 ka BP, in opposition to the rapid change in the
274 Greenland record, but interestingly enough also opposite to the local MAAT_{RC} . We attribute this to
275 the development of an even more equable hydroclimate throughout the year, with an increased
276 relative influence of 'dry'-season rainfall with higher δD values, sourced from the Gulf of Thailand
277 and the South China Sea.

278 279 *Orbital forcing of Holocene and deglacial climate*

280 After 11 kyr BP, $\delta\text{D}_{\text{wax}}$ and MAAT_{RC} vary again in tandem. Both show a generally asymptotic trend
281 towards the warmest and wettest conditions peaking at ~4.5 ka BP. This indicates that the 'steam
282 engine of the world', the IPWP, was at full power during the mid-Holocene thermal maximum,
283 exporting greatest amounts of latent heat, i.e. moisture, to the Northern Hemisphere during this
284 time. This long-term coupling between δD and MAAT_{RC} at orbital to millennial scales is opposite to
285 that of higher frequency relationships at annual to decadal scales (Fig. 2), where the total insolation
286 is distributed between latent and sensible heat. Orbital-scale changes in the seasonal distribution
287 of insolation apparently steer MAAT_{RC} and convective strength in the same direction. The
288 precessional cycle has indeed long been identified as the dominant component of orbital forcing
289 influencing tropical and monsoonal climate (e.g. 29). NH summer insolation (JJA) is most
290 commonly used to explain the waxing and waning of monsoon strength, even though leads and

291 lags between proxy records exist. In the tropics, however, the season of most intense rainfall does
292 not occur during JJA. Thus, we compare our records with 'wet season' insolation (WSI), i.e. the
293 mean monthly insolation during the wettest part of the annual cycle at 8°N. Indeed, δD_{wax} follows
294 the insolation curve for the wettest months, September-November (Fig. 4) (50), although with a
295 notable excursion during the Bø/Al-YD periods, which were caused by the influence of Sundaland.
296

297 The 7% variation of WSI over the last 18,000 years (418 - 446 kW/m²) (50) thus appears to be a
298 main driver of both surface (temperature) and atmospheric (latent, convective) heat flux. This
299 observation is consistent with a Borneo (4°N) speleothem record (51), where $\delta^{18}O$ is correlated with
300 the wettest months at that latitude (Fig. 4). The δD_{wax} record from Lake Towuti (Sulawesi) has been
301 interpreted as being driven primarily by changes in moisture source and air trajectories (52), but it
302 also shows a strong correspondence with WSI at 2°S (Dec&Jan, during the passing of the ITCZ)
303 (Fig. 4). Both δD_{wax} records (NTP and Towuti) show a sensitivity to WSI of -1.4‰ per W/m², as
304 does the Borneo record when scaled by a factor of eight for $\delta^{18}O$ according to the global meteoric
305 water line. Combined, these records provide further evidence for the influence of the precessional
306 cycle on the isotopic composition of regional precipitation, via the combined mechanisms of
307 regional convective activity and associated amount of precipitation. This is exacerbated by
308 secondary effects of seasonality, which also affects the distribution between latent and sensible
309 heat. In the tropics there is a clear correlation between insolation and rainfall amount, with at
310 present lowest values in June and July (68). Over the course of a precessional cycle, the shift in
311 seasonal distribution of solar energy can be as much as 15%, which must be causing a large effect
312 on rainfall seasonality. The lowest δD_{wax} values in the mid Holocene indicate strongest convective
313 activity during the autumn, i.e. at highest WSI, but precipitation was likely lower in spring at low
314 insolation level, causing a stronger bias in the annual mean towards the autumn. At the same time,
315 the highest MAATs observed at NTP in the mid Holocene are likely caused by a shift to mean dryer
316 conditions with clearer skies during winter and spring, even with relatively lower insolation levels.
317 At the same time, higher mid Holocene MAATs result from a combination of drier and sunnier spring
318 months, compensating for relatively low insolation levels (more sensible heat, less latent heat), and
319 cloudy wet months that however receive highest solar inputs. Our data are thus consistent with the
320 theory that the precessional cycle caused greater seasonality in the mid Holocene, compared to
321 the low-seasonality period we currently experience. The seasonal bias on the mean annual isotopic
322 composition outlined here may explain many water isotope records from the tropics, without a large
323 need to infer changes in rainfall amount, or changes in moisture source. We discuss the interaction
324 between precession and the annual cycle and its influence on precipitation seasonality and the
325 mean annual isotope signal, together with MAAT, in further detail in the supplementary information
326 (SI).
327

328 *Influence of IPWP hydroclimate on the Asian monsoon and ENSO*

329 The trends in the NTP δD_{wax} record are similar to those in the Asian speleothem $\delta^{18}O$ records
330 (53)(54) (Fig. 5), including the OD event and the 'peak isotope' feature at the beginning of the Al.
331 NTP δD_{wax} also tracks the Greenland ice core record (Fig. 5), reflecting the impact of high-latitude
332 NH forcing on tropical climate. NTP receives most of its moisture from the Indian Ocean, in contrast
333 to the East Asian speleothems, which also receive significant summer monsoon moisture from the
334 East (27)(54). The shared patterns of variation are consistent with modeling studies (55)(56), which
335 have shown that East Asian speleothem $\delta^{18}O$ records reflect the isotopic composition of the
336 advected moisture, as much or more so than rainfall amount, and that large-scale convection
337 patterns are the main drivers of the isotopic composition of precipitation (27). Our results, which
338 are similar to those from a recent study in northern Thailand (8), demonstrate that the exposure
339 and inundation of Sundaland played a decisive role in affecting the water isotopic composition not
340 across mainland East Asia, but also in Thailand. The same factors that lowered δD_{wax} at our site
341 (more rainout and more land-derived moisture from Sundaland, and greater seasonality), must also
342 have applied further inland. Remote processes upstream of the SE Asian Monsoon, such as the
343 presence / inundation of Sundaland, as well as precession-forced changes in WSI in the lower

344 tropics, need to be considered when interpreting SE Asian water isotope records in sediments
345 and speleothems. Experiments with isotope-enabled general circulation models are needed to gain
346 further insight.
347

348 Another notable feature of the δD_{wax} record are the positive ('dry') excursions between 4 and 3 ka
349 BP, which is coincident with the onset of the Meghalayan age (Fig. 3), characterized by
350 megadroughts observed in multiple regions (57). The dry events occur on top of a general decline
351 in convective activity, which follows the decrease in WSI after 5 ka BP. Our results of a wettest and
352 warmest mid Holocene extend the finding (58) of a warmer mid Holocene thermocline in the IPWP
353 east of 115°E, caused by greater September insolation. The warmer and deeper thermocline
354 causes a stronger zonal thermal difference across the equatorial Pacific, which further promotes
355 deep atmospheric convection and rainfall over western equatorial Pacific in a positive feedback
356 mechanism, inducing a stronger Walker circulation and suppression of ENSO activity. The
357 interaction of the precessional and seasonal cycles that act upon the IPWP, being the 'steam
358 engine of the world', thus appears to play a decisive role in global climate dynamics by regulating
359 the amount of latent heat exported to the higher latitudes. In this respect, we even speculate that
360 the inundation and warming of Sundaland and may have provided a key positive feedback
361 mechanism during the last G-I transition, and possibly also earlier ones.
362

363
364

365 **Materials and Methods**

366
367

367 *Sampling and sample processing*

368 Two parallel sediment cores were retrieved in one-meter sections using a rod-operated Russian
369 corer from a small raft at the deepest part of the lake. After recovery, the sections were wrapped in
370 foil and secured and transported in PVC tubes to Stockholm University, where they were stored at
371 4°C until further analysis. Sub-samples were taken in contiguous 1-cm increments and split to
372 accommodate subsequent analyses. One half of the samples was utilized for macrofossil and
373 charcoal analysis and radiocarbon dating. The other half of the samples was freeze-dried and
374 analysed for loss-on-ignition (LOI), bulk total organic carbon (TOC), nitrogen (TN) and their
375 isotopes, lipid biomarkers and compound-specific hydrogen and carbon isotopes. For LOI, samples
376 were dried overnight at 105°C, ground and then combusted at 550 °C for 3h. LOI was calculated
377 as a percentage of the dry sample weight to obtain an estimate of the organic matter and carbonate
378 content. In parallel, a sediment-water interface surface core covering the last 150 years was
379 retrieved and sampled on site in one cm slices (17).
380

381
382

382 *Macrofossil analysis and radiocarbon dating*

383 Approximately 380 samples were sieved under running water (mesh sizes 0.5 and 0.25 mm) to
384 recover plant macrofossils for radiocarbon dating. Plant remains were picked with tweezers under
385 a binocular microscope, described, and rinsed multiple times in deionized water, placed in pre-
386 cleaned glass vials and dried overnight at 105 °C. 59 samples were dated at the 14Chrono Centre,
387 Queen's University Belfast, where pre-treatment and measurement followed the methodology
388 described in (59). Based on these, an age-model (SI Fig. 1) was constructed using Bacon, a
389 Bayesian statistics-based routine (60) that estimates the accumulation rate for sediment segments
390 based on the radiocarbon dates calibrated using the intCal13 NH calibration curve (61).
391

392
393

393 *Bulk geochemistry*

394 %TOC, %TN and bulk $\delta^{13}C_{org}$ and bulk $\delta^{15}N_{bulk}$ were measured on a Carlo Erba NC2500 elemental
395 analyser, coupled to a Finnigan MAT Delta⁺ mass spectrometer. To remove carbonates, samples
396 were fumigated with HCl within a dessicator prior to analysis. $\delta^{13}C_{bulk}$ is expressed in ‰ against the
397 Vienna PeeDee Belemnite (VPDB) standard, and had an analytical error of less than $\pm 0.15\%$.
 $\delta^{15}N_{bulk}$ are reported in ‰ relative to air (N), with an analytical error of $\pm 0.15\%$.

398 *Lipid biomarkers*

399 Lipid extraction was performed on freeze-dried samples by sonication with a mixture of
400 dichloromethane and methanol (DCM-MeOH 9:1 v/v) for 20 minutes and subsequent
401 centrifugation. The process was repeated three times and supernatants were combined. Aliphatic
402 hydrocarbon fractions were isolated from the total lipid extract using silica gel columns (5%
403 deactivated) that were first eluted with pure hexane (F1) and subsequently with a mixture of DCM-
404 MeOH (1:1 v/v) to obtain a polar fraction (F2). A saturated hydrocarbon fraction was obtained by
405 eluting the F1 fraction through 10% AgNO₃ impregnated silica gel using pure hexane as eluent.
406 The saturated hydrocarbon fractions were analyzed by gas chromatography – mass spectrometry
407 for identification and quantification, using a Shimadzu GCMS-QP2010 Ultra. C₂₁ to C₃₃ *n*-alkanes
408 were identified based on mass spectra from the literature and retention times. The concentrations
409 of individual compounds were determined using a calibration curve made using mixtures of C₂₁-C₄₀
410 alkanes of known concentration.

411

412 *Leaf wax hydrogen and carbon isotope analysis*

413 The hydrogen isotopic composition of *n*-alkanes (expressed in delta notation in ‰ against VSMOW)
414 was analyzed by gas chromatography–isotope ratio monitoring–mass spectrometry (GC-IRMS)
415 using a Thermo Finnigan Delta V mass spectrometer interfaced with a Thermo Trace GC 2000
416 using the HTC reactor of a GC Isolink II and Conflo IV system. Helium was used as a carrier gas
417 at constant flow mode and the compounds separated on a Zebron ZB-5HT Inferno GC column (30
418 m x 0.25 mm x 0.25 μm). A standard set of alkanes with known isotopic composition (obtained from
419 A. Schimmelmann, Indiana University, USA) was used for daily calibration of the reference gas.
420 The average standard deviation of δD values was 5‰. The reported δD_{wax} values are the average
421 of the most abundant long chain *n*-alkanes: C₂₇, C₂₉ and C₃₁. To correct for the higher global
422 average of global oceanic δD during lower sea levels, the δD values of the *n*-alkanes were ice
423 volume corrected (*c.f.* (41) as follows: δD_{wax-c} = (δD_{wax} + 1000) / (δO¹⁸_w * 8 * 0.001 + 1) - 1000, with
424 interpolated ocean water δO¹⁸_w values (62).

425 δ¹³C_{wax} was measured on the same compounds on the same system and the same isotope
426 standards, except for the use of the combustion reactor. δ¹³C_{wax} values are the average of C₂₇, C₂₉
427 and C₃₁ alkanes, expressed in delta notation in ‰ against VPDB, with an average standard
428 deviation of 0.5‰.

429

430 *Glycerol dialkyl glycerol tetraether (GDGT) analysis*

431 Branched glycerol dialkyl glycerol tetraethers (brGDGTs) were measured on the F2 fractions after
432 reconstituting in MeOH:DCM 9:1 and subsequent filtration through 0.45 μm PTFE filters, following
433 published protocols (63). Analysis was done using a Thermo-Dionex HPLC connected to a Thermo
434 Scientific TSQ quantum access triple quadrupole mass spectrometer, using an APCI interface.
435 Chromatographic separation was achieved on a Kinetex C18-XB reverse phase column using a
436 gradient of mobile phase A: MeOH with 0.04% formic acid and mobile phase B: propan-2-ol with
437 0.04% formic acid. GDGTs were detected in SIM mode at *m/z* 1020 (scan width 7, 0.2s), 1034
438 (width 7, 0.2s), 1048 (width 7, 0.2s), 1296 (width 17.5, 0.5s). Quantification was performed using
439 Excalibur software, using the (M+) and (M+1) ions of the GDGTs. More details can be found
440 elsewhere (63). MBT and CBT proxies were calculated following (64).

441

442

443 **Acknowledgments**

444

445 This work was supported by Swedish Research Council (VR) research grants 621-2008-2855 to
446 RHS and 348-2008-6071 and 621-2011-4916 to BW. We wish to thank Sherilyn Fritz,
447 Wichuratree Klubseang and Sudo Inthonkaew for sampling assistance and discussion. Jayne
448 Rattray and Anna Hägglund and Camilla Bredberg are thanked for laboratory assistance. Paula
449 Reimer from Queen's University of Belfast conducted the radiocarbon analyses.

450

451 The data presented in this paper is available online at the Bolin Centre of Climate Research
452 Database: (link).

453

454

455

456 **References**

457

- 458 1. P. De Deckker, The Indo-Pacific Warm Pool: critical to world oceanography and world
459 climate. *Geoscience Letters* **3**, 20 (2016).
- 460 2. A. Timmermann, *et al.*, El Niño–Southern Oscillation complexity. *Nature* **559**, 535–545
461 (2018).
- 462 3. M. Mohtadi, M. Prange, E. Schefuß, T. C. Jennerjahn, Late Holocene slowdown of the Indian
463 Ocean Walker circulation. *Nat Commun* **8**, 1–8 (2017).
- 464 4. J. T. Randerson, *et al.*, Fire emissions from C3 and C4 vegetation and their influence on
465 interannual variability of atmospheric CO₂ and δ¹³CO₂. *Global Biogeochemical Cycles* **19**
466 (2005).
- 467 5. A. Koutavas, S. Joannides, El Niño-Southern Oscillation extrema in the Holocene and Last
468 Glacial Maximum: ENSO EXTREMA IN THE HOLOCENE AND LGM. *Paleoceanography* **27**
469 (2012).
- 470 6. P. N. DiNezio, J. E. Tierney, The effect of sea level on glacial Indo-Pacific climate. *Nature*
471 *Geosci* **6**, 485–491 (2013).
- 472 7. P. N. Di Nezio, *et al.*, The climate response of the Indo-Pacific warm pool to glacial sea level.
473 *Paleoceanography* **31**, 866–894 (2016).
- 474 8. K. A. Yamoah, *et al.*, A muted El Niño-like condition during late MIS 3. *Quaternary Science*
475 *Reviews* **254**, 106782 (2021).
- 476 9. X. Wang, X. Sun, P. Wang, K. Stattegger, Vegetation on the Sunda Shelf, South China Sea,
477 during the Last Glacial Maximum. *Palaeogeography, Palaeoclimatology, Palaeoecology*
478 **278**, 88–97 (2009).
- 479 10. L. X. Sun Xiang Jun, L. X. Sun Xiang Jun, Vegetation and Climate on the Sunda Shelf of the
480 South China Sea During the Last Glaciation-Pollen Results from Station 17962. *J Integr*
481 *Plant Biol* **44** (2002).
- 482 11. N. Dubois, *et al.*, Indonesian vegetation response to changes in rainfall seasonality over the
483 past 25,000 years. *Nature Geoscience* **7**, 513–517 (2014).
- 484 12. J. W. Partin, K. M. Cobb, J. F. Adkins, B. Clark, D. P. Fernandez, Millennial-scale trends in
485 west Pacific warm pool hydrology since the Last Glacial Maximum. *Nature* **449**, 452–455
486 (2007).
- 487 13. C. M. Wurster, H. Rifai, B. Zhou, J. Haig, M. I. Bird, Savanna in equatorial Borneo during the
488 late Pleistocene. *Sci Rep* **9**, 1–7 (2019).
- 489 14. L. R. Heaney, A synopsis of climatic and vegetational change in Southeast Asia. *Climatic*
490 *Change* **19**, 53–61 (1991).
- 491 15. C. M. Wurster, *et al.*, Forest contraction in north equatorial Southeast Asia during the Last
492 Glacial Period. *Proceedings of the National Academy of Sciences* **107**, 15508–15511 (2010).
- 493 16. S Snansieng, Gitsan, N, P. Sripongnan, Geological map of Changwat Nakhon Si Thammarat.
494 (1976).
- 495 17. K. A. Yamoah, *et al.*, A 150-year record of phytoplankton community succession controlled
496 by hydroclimatic variability in a tropical lake. *Biogeosciences* **13**, 3971–3980 (2016).

- 497 18. H. Pinto, R. E. Sharwood, D. T. Tissue, O. Ghannoum, Photosynthesis of C3, C3–C4, and C4
498 grasses at glacial CO₂. *J Exp Bot* **65**, 3669–3681 (2014).
- 499 19. D. Sachse, *et al.*, Molecular Paleohydrology: Interpreting the Hydrogen-Isotopic
500 Composition of Lipid Biomarkers from Photosynthesizing Organisms. *Annu. Rev. Earth*
501 *Planet. Sci.* **40**, 221–249 (2012).
- 502 20. J. M. Russell, E. C. Hopmans, S. E. Loomis, J. Liang, J. S. S. Damsté, Distributions of 5- and 6-
503 methyl branched glycerol dialkyl glycerol tetraethers (brGDGTs) in East African lake
504 sediment: Effects of temperature, pH, and new lacustrine paleotemperature calibrations.
505 *Organic Geochemistry* **117**, 56–69 (2018).
- 506 21. S. Schouten, E. C. Hopmans, J. S. Sinninghe Damsté, The organic geochemistry of glycerol
507 dialkyl glycerol tetraether lipids: A review. *Organic Geochemistry* **54**, 19–61 (2013).
- 508 22. Q. Sun, *et al.*, Distributions and temperature dependence of branched glycerol dialkyl
509 glycerol tetraethers in recent lacustrine sediments from China and Nepal. *Journal of*
510 *Geophysical Research: Biogeosciences* **116** (2011).
- 511 23. S. Bony, C. Risi, F. Vimeux, Influence of convective processes on the isotopic composition (δ
512 ¹⁸O and δ D) of precipitation and water vapor in the tropics: 1. Radiative-convective
513 equilibrium and Tropical Ocean–Global Atmosphere–Coupled Ocean–Atmosphere
514 Response Experiment (TOGA-COARE) simulations. *J. Geophys. Res.* **113**, D19305 (2008).
- 515 24. D. Sachse, J. Radke, G. Gleixner, Hydrogen isotope ratios of recent lacustrine sedimentary n-
516 alkanes record modern climate variability. *Geochimica et Cosmochimica Acta* **68**, 4877–
517 4889 (2004).
- 518 25. A. L. Sessions, T. W. Burgoyne, A. Schimmelmann, J. M. Hayes, Fractionation of hydrogen
519 isotopes in lipid biosynthesis. *Organic Geochemistry* **30**, 1193–1200 (1999).
- 520 26. S. J. Feakins, *et al.*, Plant leaf wax biomarkers capture gradients in hydrogen isotopes of
521 precipitation from the Andes and Amazon. *Geochimica et Cosmochimica Acta* **182**, 155–
522 172 (2016).
- 523 27. Z. Wei, *et al.*, Influences of large-scale convection and moisture source on monthly
524 precipitation isotope ratios observed in Thailand, Southeast Asia. *Earth and Planetary*
525 *Science Letters* **488**, 181–192 (2018).
- 526 28. A. H. Sobel, E. D. Maloney, G. Bellon, D. M. Frierson, Surface fluxes and tropical
527 intraseasonal variability: A reassessment. *Journal of Advances in Modeling Earth Systems* **2**
528 (2010).
- 529 29. C. Jalihal, J. H. C. Bosmans, J. Srinivasan, A. Chakraborty, The response of tropical
530 precipitation to Earth’s precession: the role of energy fluxes and vertical stability. *Clim.*
531 *Past* **15**, 449–462 (2019).
- 532 30. W. M. Lewis Jr, Tropical lakes: how latitude makes a difference. *Perspectives in tropical*
533 *limnology* **4364** (1996).
- 534 31. J. E. Tierney, *et al.*, Glacial cooling and climate sensitivity revisited. *Nature* **584**, 569–573
535 (2020).
- 536 32. S. C. Porter, Snowline depression in the tropics during the Last Glaciation. *Quaternary*
537 *Science Reviews* **20**, 1067–1091 (2000).
- 538 33. Y. Garcin, *et al.*, Reconstructing C3 and C4 vegetation cover using n-alkane carbon isotope
539 ratios in recent lake sediments from Cameroon, Western Central Africa. *Geochimica et*
540 *Cosmochimica Acta* **142**, 482–500 (2014).
- 541 34. J. R. Ehleringer, T. E. Cerling, B. R. Helliker, C4 photosynthesis, atmospheric CO₂, and
542 climate. *Oecologia* **112**, 285–299 (1997).

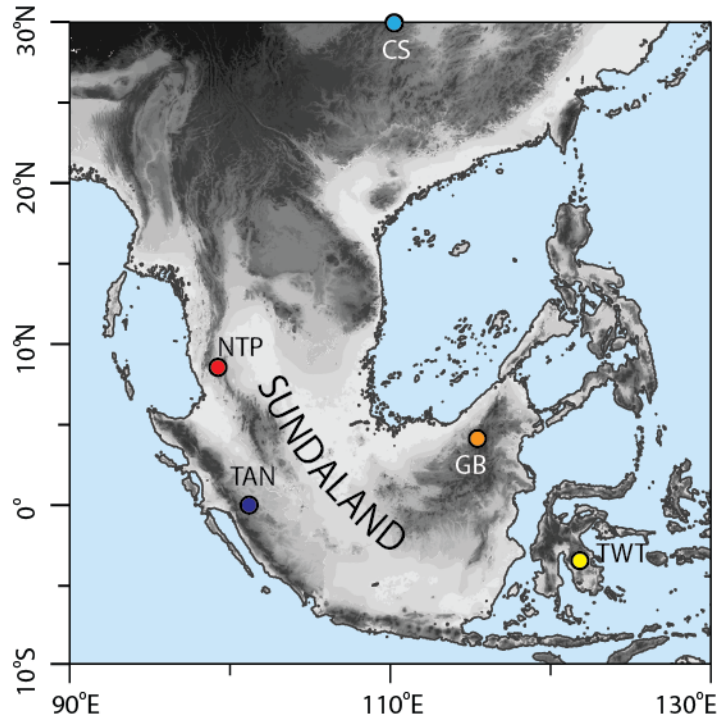
- 543 35. G. J. Collatz, J. A. Berry, J. S. Clark, Effects of climate and atmospheric CO₂ partial pressure
544 on the global distribution of C₄ grasses: present, past, and future. *Oecologia* **114**, 441–454
545 (1998).
- 546 36. T. E. Cerling, J. R. Ehleringer, J. M. Harris, Carbon dioxide starvation, the development of C₄
547 ecosystems, and mammalian evolution. *Phil. Trans. R. Soc. Lond. B* **353**, 159–171 (1998).
- 548 37. J. S. Sinninghe Damsté, *et al.*, A 25,000-year record of climate-induced changes in lowland
549 vegetation of eastern equatorial Africa revealed by the stable carbon-isotopic composition
550 of fossil plant leaf waxes. *Earth and Planetary Science Letters* **302**, 236–246 (2011).
- 551 38. F. A. Street-Perrott, Impact of Lower Atmospheric Carbon Dioxide on Tropical Mountain
552 Ecosystems. *Science* **278**, 1422–1426 (1997).
- 553 39. V. J. Hare, E. Loftus, A. Jeffrey, C. B. Ramsey, Atmospheric CO₂ effect on stable carbon
554 isotope composition of terrestrial fossil archives. *Nature Communications* **9** (2018).
- 555 40. A. F. Diefendorf, E. J. Freimuth, Extracting the most from terrestrial plant-derived n-alkyl
556 lipids and their carbon isotopes from the sedimentary record: A review. *Organic*
557 *Geochemistry* **103**, 1–21 (2017).
- 558 41. J. E. Tierney, P. B. deMenocal, Abrupt Shifts in Horn of Africa Hydroclimate Since the Last
559 Glacial Maximum. *Science* **342**, 843–846 (2013).
- 560 42. W. Liu, H. Yang, Multiple controls for the variability of hydrogen isotopic compositions in
561 higher plant n-alkanes from modern ecosystems: variability of hydrogen isotopic
562 compositions. *Global Change Biology* **14**, 2166–2177 (2008).
- 563 43. Y. V. Wang, *et al.*, What does leaf wax δD from a mixed C₃/C₄ vegetation region tell us?
564 *Geochimica et Cosmochimica Acta* **111**, 128–139 (2013).
- 565 44. T. J. J. Hanebuth, H. K. Voris, Y. Yokoyama, Y. Saito, J. Okuno, Formation and fate of
566 sedimentary depocentres on Southeast Asia's Sunda Shelf over the past sea-level cycle and
567 biogeographic implications. *Earth-Science Reviews* **104**, 92–110 (2011).
- 568 45. B. P. Murphy, D. M. J. S. Bowman, Seasonal water availability predicts the relative
569 abundance of C₃ and C₄ grasses in Australia. *Global Ecol Biogeography* **16**, 160–169
570 (2007).
- 571 46. J. M. Russell, *et al.*, Glacial forcing of central Indonesian hydroclimate since 60,000 y B.P.
572 *Proceedings of the National Academy of Sciences* **111**, 5100–5105 (2014).
- 573 47. P. M. J. Douglas, M. Pagani, M. Brenner, D. A. Hodell, J. H. Curtis, Aridity and vegetation
574 composition are important determinants of leaf-wax δD values in southeastern Mexico
575 and Central America. *Geochimica et Cosmochimica Acta* **97**, 24–45 (2012).
- 576 48. X. Yuan, M. R. Kaplan, M. A. Cane, The Interconnected Global Climate System—A Review of
577 Tropical–Polar Teleconnections. *J. Climate* **31**, 5765–5792 (2018).
- 578 49. A. C. Clement, R. Seager, M. A. Cane, Orbital controls on the El Niño/Southern Oscillation
579 and the tropical climate. *Paleoceanography* **14**, 441–456 (1999).
- 580 50. J. Laskar, *et al.*, A long-term numerical solution for the insolation quantities of the Earth.
581 *A&A* **428**, 261–285 (2004).
- 582 51. S. Chen, *et al.*, A high-resolution speleothem record of western equatorial Pacific rainfall:
583 Implications for Holocene ENSO evolution. *Earth and Planetary Science Letters* **442**, 61–71
584 (2016).
- 585 52. B. Konecky, J. Russell, S. Bijaksana, Glacial aridity in central Indonesia coeval with intensified
586 monsoon circulation. *Earth and Planetary Science Letters* **437**, 15–24 (2016).
- 587 53. H. Cheng, *et al.*, The Asian monsoon over the past 640,000 years and ice age terminations.
588 *Nature* **534**, 640–646 (2016).

- 589 54. Zhang, *et al.*, The Asian Summer Monsoon: Teleconnections and Forcing Mechanisms—A
590 Review from Chinese Speleothem $\delta^{18}\text{O}$ Records. *Quaternary* **2**, 26 (2019).
- 591 55. X. Yang, *et al.*, Holocene stalagmite $\delta^{18}\text{O}$ records in the East Asian monsoon region and
592 their correlation with those in the Indian monsoon region. *The Holocene* **24**, 1657–1664
593 (2014).
- 594 56. F. S. R. Pausata, D. S. Battisti, K. H. Nisancioglu, C. M. Bitz, Chinese stalagmite $\delta^{18}\text{O}$
595 controlled by changes in the Indian monsoon during a simulated Heinrich event. *Nature*
596 *Geosci* **4**, 474–480 (2011).
- 597 57. G. Kathayat, *et al.*, Evaluating the timing and structure of the 4.2ka event in the Indian
598 summer monsoon domain from an annually resolved speleothem record from Northeast
599 India. *Climate of the Past* **14**, 1869–1879 (2018).
- 600 58. H. Dang, *et al.*, Pacific warm pool subsurface heat sequestration modulated Walker
601 circulation and ENSO activity during the Holocene. *Sci. Adv.* **6**, eabc0402 (2020).
- 602 59. S. Chawchai, *et al.*, Hydroclimatic shifts in northeast Thailand during the last two millennia –
603 the record of Lake Pa Kho. *Quaternary Science Reviews* **111**, 62–71 (2015).
- 604 60. M. Blaauw, J. A. Christen, Flexible paleoclimate age-depth models using an autoregressive
605 gamma process. *Bayesian Anal.* **6**, 457–474 (2011).
- 606 61. P. J. Reimer, *et al.*, IntCal13 and Marine13 Radiocarbon Age Calibration Curves 0–50,000
607 Years cal BP. *Radiocarbon* **55**, 1869–1887 (2013).
- 608 62. C. Waelbroeck, *et al.*, Sea-level and deep water temperature changes derived from benthic
609 foraminifera isotopic records. *Quaternary Science Reviews* **21**, 295–305 (2002).
- 610 63. J. E. Rattray, R. H. Smittenberg, Separation of Branched and Isoprenoid Glycerol Dialkyl
611 Glycerol Tetraether (GDGT) Isomers in Peat Soils and Marine Sediments Using Reverse
612 Phase Chromatography. *Front. Mar. Sci.* **7** (2020).
- 613 64. J. W. H. Weijers, S. Schouten, J. C. van den Donker, E. C. Hopmans, J. S. Sinninghe Damsté,
614 Environmental controls on bacterial tetraether membrane lipid distribution in soils.
615 *Geochimica et Cosmochimica Acta* **71**, 703–713 (2007).
- 616 65. I. Harris, T. J. Osborn, P. Jones, D. Lister, Version 4 of the CRU TS monthly high-resolution
617 gridded multivariate climate dataset. *Scientific Data* **7**, 1–18 (2020).
- 618 66. E. Monnin, EPICA Dome C high resolution carbon dioxide concentrations (2006)
619 <https://doi.org/10.1594/PANGAEA.472488> (January 6, 2021).
- 620 67. K. K. Andersen, *et al.*, High-resolution record of Northern Hemisphere climate extending
621 into the last interglacial period. *Nature* **431**, 147–151 (2004).
- 622 68. J. B. Wurtzel, *et al.*, Tropical Indo-Pacific hydroclimate response to North Atlantic forcing
623 during the last deglaciation as recorded by a speleothem from Sumatra, Indonesia. *Earth*
624 *and Planetary Science Letters* **492**, 264–278 (2018).
- 625
626
627

628 **Figures**

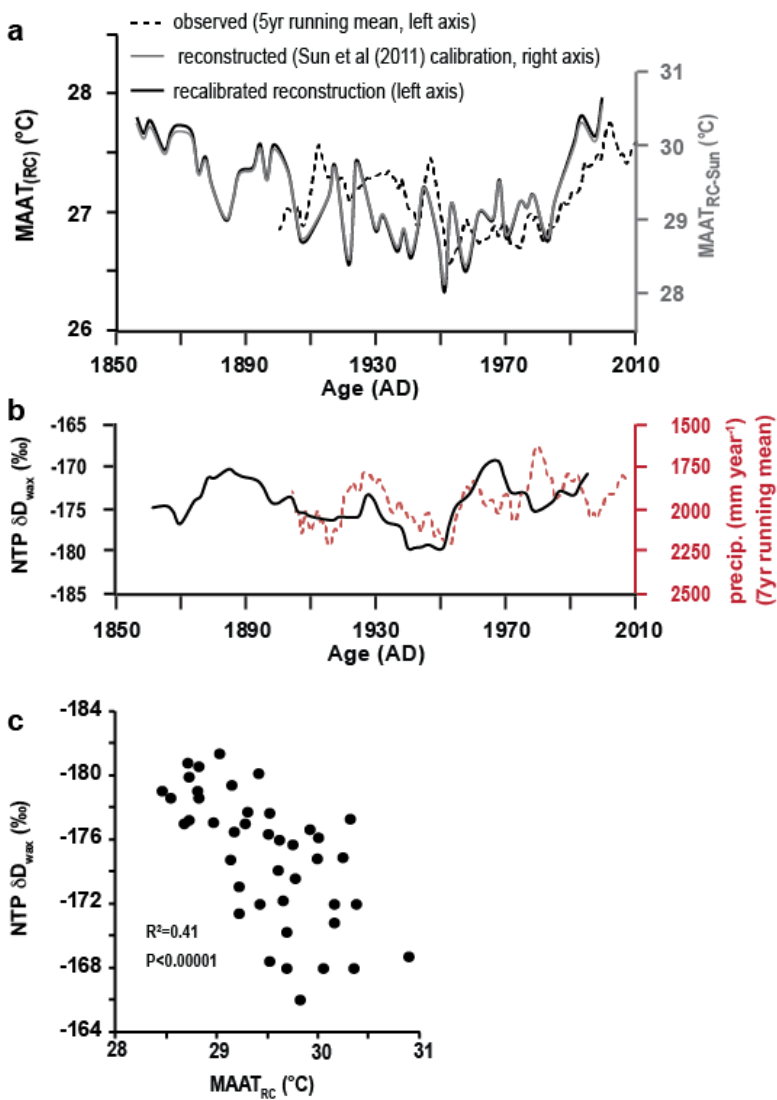
629

630 **Figure 1.** Location of Lake Nong Thale Prong (NTP) and other records mentioned in the text: GB:
631 Gunung Buda National Park speleothem, Borneo; TWT: Lake Towuti, Sulawesi; CS: Chinese
632 Speleothems; TAN: Tangga cave, Sumatra. The map shows the extent of the emerged
633 landscapes of former Sundaland during the last glacial maximum sea level low stand.
634



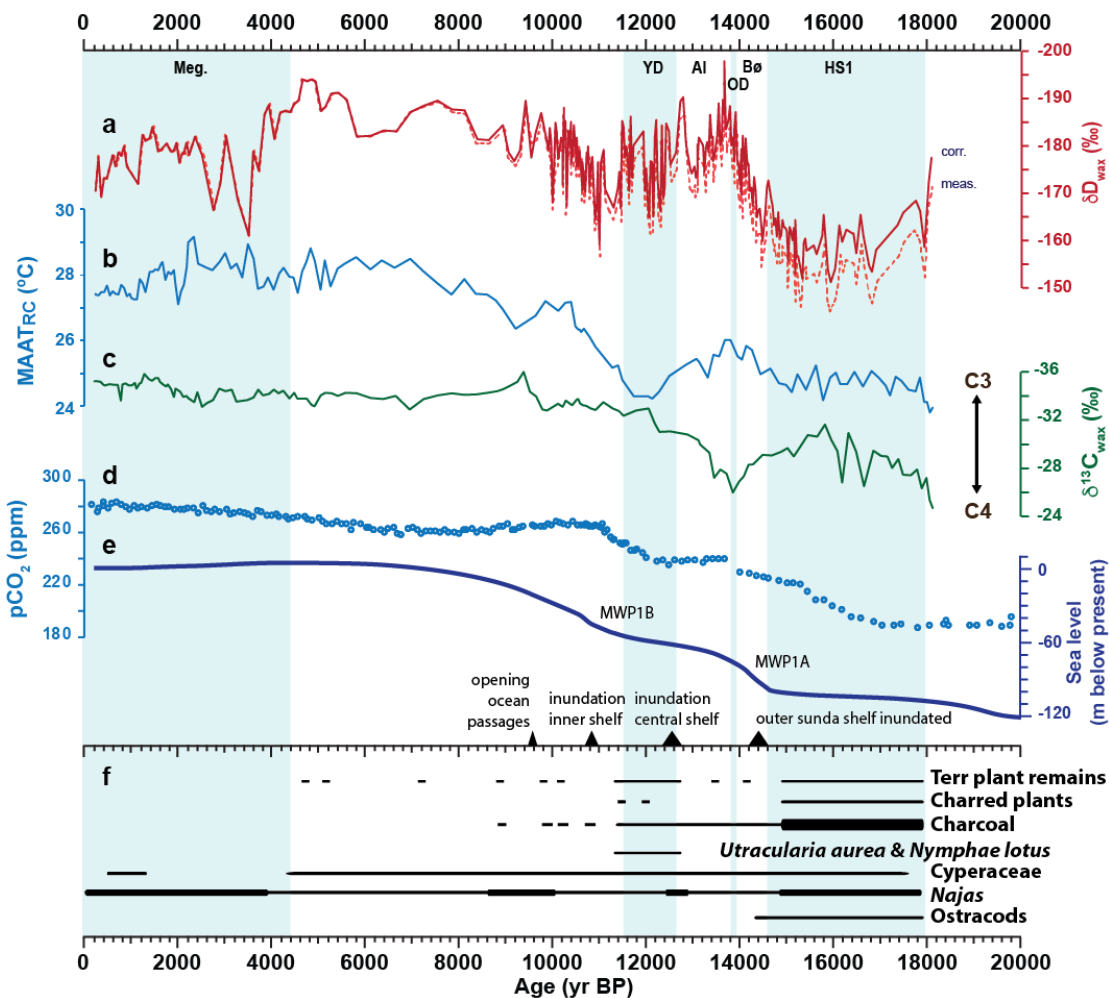
635

636 **Figure 2.** Comparison of instrumental climate data with proxy data measured on the NTP surface
 637 sediments. **a)** Mean Annual Air Temperature (MAAT_{RC-Sun}) reconstructed using bacterial-derived
 638 branched GDGTs (right axis, grey), compared to observations (left axis, stippled black). To obtain
 639 a local calibration the reconstructed MAAT was scaled for amplitude and mean (see SI) to
 640 correspond with the instrumental record (black, left axis). **b)** Instrumental rainfall data (right axis,
 641 stippled red) compared with δD_{wax} data from the same samples (17) suggests a good correlation
 642 between the two. **c)** Scatter plot of δD_{wax} and reconstructed MAAT from the same samples.
 643 Instrumental climate data are taken from the CRU TS monthly high-resolution gridded multivariate
 644 climate dataset, Version 4 (65).
 645



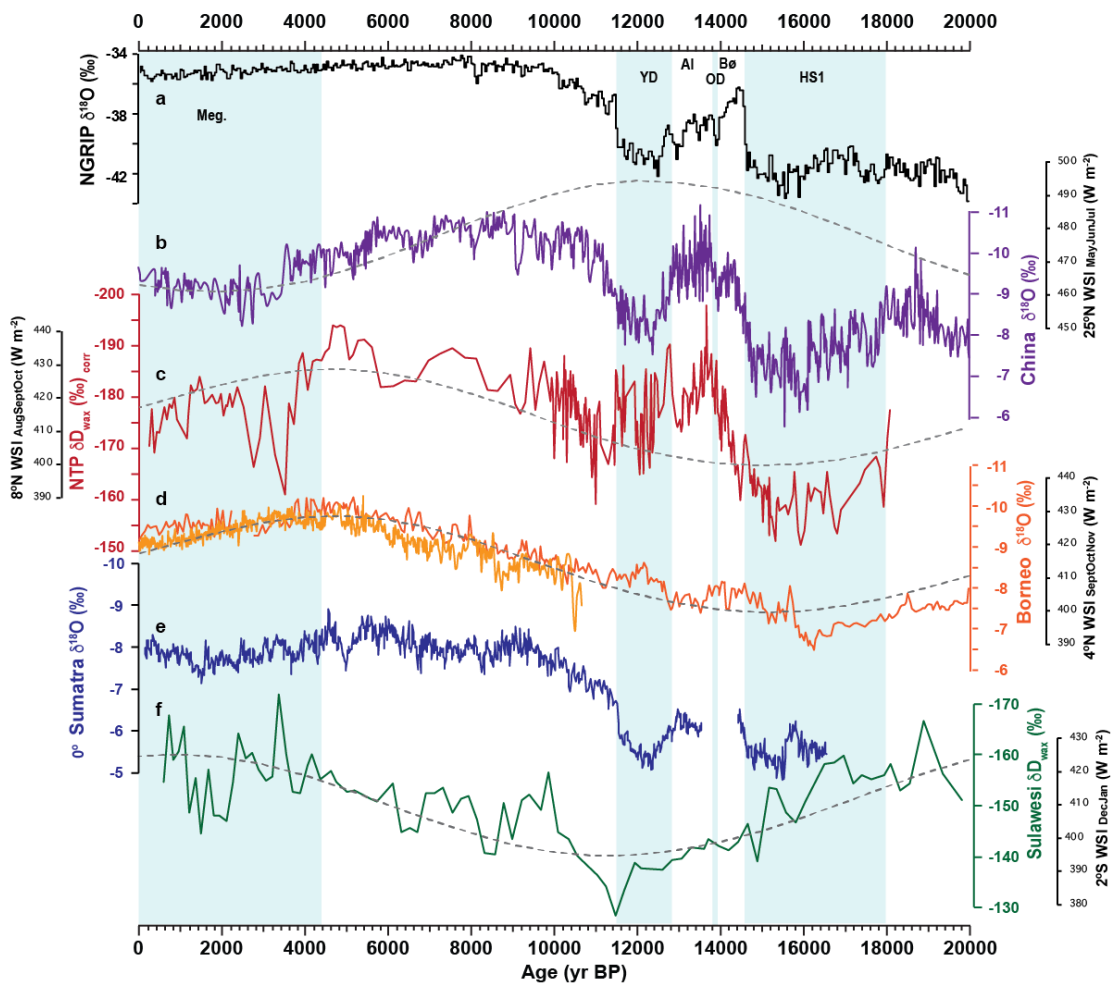
646

647 **Figure 3.** Proxy records of lake NTP of the last 18,000 years. **a)** δD_{wax} , both as measured and
 648 corrected (stippled) for global sea level change. **b)** Reconstructed mean annual air temperature
 649 (MAAT_{RC}). **c)** $\delta^{13}C_{wax}$. **d)** Atmospheric CO₂ levels (66). **e)** Sea level reconstruction for the Sunda
 650 Shelf region (44) **f)** Macrofossil and charcoal results. Thick line: very abundant; Thin line: present.
 651 Meg: Meghalayan period; YD: Younger Dryas; AI: Allerød; OD: Older Dryas; Bø: Bølling; HS1:
 652 Heinrich Stadial 1. MWP: Meltwater pulses.



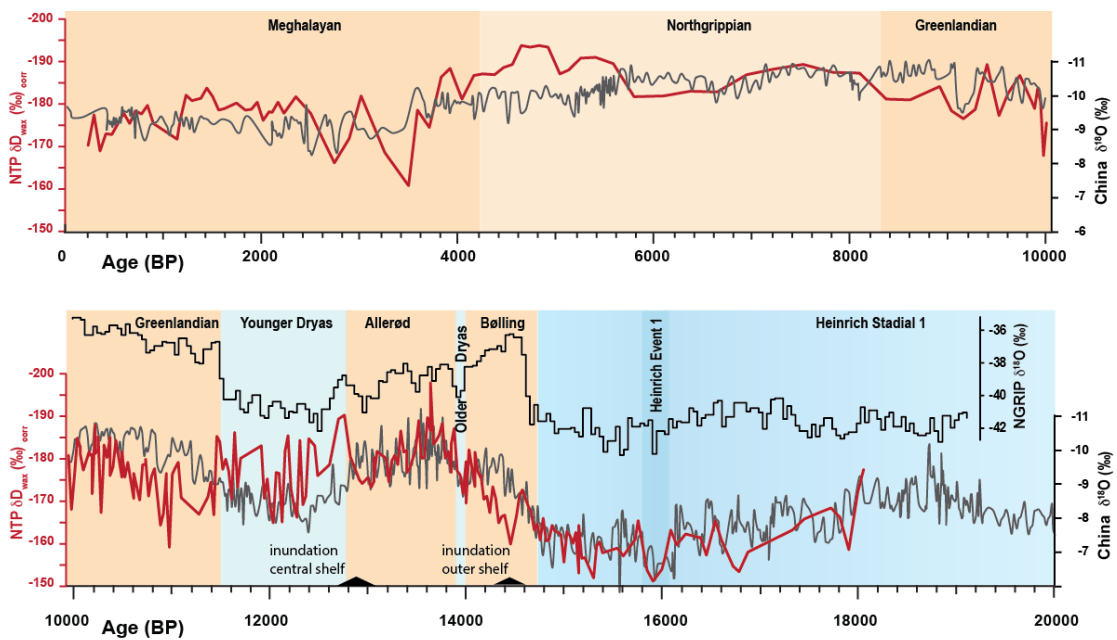
654

655 **Figure 4.** Comparison of isotope records. **a)** Greenland ice core $\delta^{18}\text{O}$ as a reference for NH
 656 temperature (67). **b)** Combined Chinese speleothem $\delta^{18}\text{O}$ (53). **c)** NTP δD_{wax} corrected for sea
 657 level effect (this study). **d)** Borneo speleothem $\delta^{18}\text{O}$ record (dark(12) and light (51) orange). **e)**
 658 Sumatra speleothem $\delta^{18}\text{O}$ record (68). **f)** Sulawesi δD_{wax} record (52). b-f are all plotted on the
 659 same scale where one unit in $\delta^{18}\text{O}$ corresponds to 8 units in δD space, according to the global
 660 meteoric water line. Grey dotted lines over b-d and f show the solar irradiation averaged for the 2
 661 or 3 wettest months (WSI:Wet Season Insolation) for the latitudes of the respective records (50).
 662 No clear wettest period could be defined for Sumatra (see SI). Time periods are shown as in in
 663 Figure 3.
 664



665

666 **Figure 5.** Comparison of the sea-level-corrected NTP δD_{wax} (this study) with the Chinese
 667 speleothem $\delta^{18}O$ record over the last 20,000 years (53) and Greenland $\delta^{18}O$ for reference (67).
 668 The records are scaled in the same way as in Figure 4.
 669



670
 671
 672

673

674 **Supplementary Information for**

675 A 18,000 yr record of tropical land temperature, convective activity
676 and rainfall seasonality from the maritime continent

677

678

679 Rienk H. Smittenberg, Kweku A. Yamoah, Frederik Schenk, Akkaneewut Chabangborn,
680 Sakonvan Chawchai, Minna Väiliranta and Barbara Wohlfarth

681

682 Corresponding authors: Rienk H. Smittenberg, Barbara Wohlfarth

683 Email: rienk.smittenberg@geo.su.se; barbara.wohlfarth@geo.su.se

684

685 **This PDF file includes:**

686 Supplementary text

687 Figures S1 to S10

688 SI References

689

690 *Other supplementary data for this manuscript will be made available at the Bolin Center*
691 *of Climate research Database: <https://bolin.su.se/data/>*

692

693 Supplementary Tables

694 Table 1. Composite stratigraphy

695 Table 2. Radiocarbon Data

696 Table 3. Plant macrofossil and charcoal data

697 Table 4. Bulk geochemistry: TOC, TN, LOI, $\delta^{13}\text{C}_{\text{bulk}}$ and $\delta^{15}\text{N}_{\text{bulk}}$

698 Table 5. Leaf wax δD

699 Table 6. Leaf wax $\delta^{13}\text{C}$

700 Table 7. GDGTs and reconstructed MAAT

701 Table 8. Surface Core GDGTs, reconstructed MAAT, leaf wax δD and instrumental

702 MAAT

703

704 Temperature reconstruction using branched GDGTs

705 A basic prerequisite for the valid use of brGDGTs, a relatively high branched-over-
706 isoprenoid tetraether (BIT) index, is easily met with values of 1.0 throughout the core.
707 Reconstructed pH values, based on the CBT index (1) were 8.0 ± 0.2 over the entire core,
708 with lowest values during the YD and a downward trend for the last 2000 years (Fig. S4).
709 This means that temperature is the dominant environmental factor exerted on the brGDGT
710 distribution. At the time of measurement, we had not adopted the new HILIC-based
711 method which separates between 5-methyl and 6-methyl branched GDGTs (2) but used
712 our own method based on reverse phase chromatography (3), similar to the one used by
713 Zhu *et al.* (4), and which compared well with the original method using a cyano column.
714 As a consequence, we do not have individual quantifications of 5-methyl and 6-methyl
715 branched GDGT isomers used in the revised MBT_{5me} temperature proxy for mineral soils
716 (5), peats (6), or East African lakes (7). However, for high temperatures as is the case for
717 our site, the main response to temperature is a shift between tetra- and pentamethylated
718 GDGTs, which makes the differentiation between 5- and 6-methyl GDGTs less relevant
719 than in cold environments. The relative abundance of tetra-, penta- and hexamethylated
720 GDGTs plot in the same region as datasets produced with the HILIC method from east
721 African lakes and from global soils and peats (Fig S4). This strengthens the confidence
722 that the brGDGTs we measured can be used as a temperature proxy. Among the various
723 GDGT-temperature calibrations that have been developed since the original one (1), we
724 chose to apply the global lake calibration of Sun *et al.* (8) for lakes with $pH < 8.5$, which also
725 included data from nearby lake Towuti:

726

$$727 \quad MAAT_{Sun-cal} = 3.949 + 38.213 MBT - 5.593 CBT \quad (\text{Eq. 1})$$

728

729 The MBT/CBT-based MAAT ($^{\circ}\text{C}$) reconstruction using the global regression model (8)
730 shows a good agreement with temperature observations in the region (closest grid point
731 at 8.25°N ; 99.25°E from the University of East Anglia Climate Research Unit dataset
732 CRU TS3.23) (9) for the overlapping period of 1903-2001. There is however an offset and
733 overestimation of variability in the proxy reconstruction using the global lake calibration
734 relative to the local temperature. To adjust the reconstruction to our local conditions, we
735 re-calibrated the global reconstruction by replacing the mean of the $MAAT_{Sun-cal}$ values
736 obtained using the global regression ($\mu_{proxy-global}$) and standard deviation ($\sigma_{proxy-global}$) with
737 those of local conditions from CRU TS3.23. This was done by first normalizing the proxy
738 record for the overlapping period 1903-2001 and then re-normalize it using the mean (μ_{obs-}
739 $local$) and standard deviation ($\sigma_{obs-local}$) of the local observations for the same time period
740 (Eq. 2).

741

$$742 \quad MAAT_{i,local} = \left[(x_{i,proxy-global} - \mu_{Proxy-global}) \frac{\sigma_{Obs-local}}{\sigma_{Proxy-global}} \right] + \mu_{Obs-local} \quad (\text{Eq. 2})$$

743

744 resulting in a record of recalibrated MAAT_{RC} values. This re-calibration effectively adjusts
745 the intercept and slope of the original calibration so that the proxy data reflects the mean
746 and annual variability observed over the instrumental record. Generating a new calibration
747 by regression of the GDGT data with the instrumental record is not straightforward,
748 because the samples do not correspond to annual measurements but approximately 3
749 years, with an error of the age estimate based on ²¹⁰Pb dating that increases with depth.

750 We even performed the same exercise using the original calibration (1), and came to the
751 same results (Fig S4a). It is important to note that all data come from one location where
752 the microbial ecology of the brGDGT-producing organisms and the dominant
753 environmental factors vary much less compared to the globally distributed surface
754 sediment datasets used to generate the GDGT calibrations. For reference, the RMSE of
755 the East African lake calibration (7) is approximately 2.5°C.

756

757

758

759 **About the influence of the precessional cycle on seasonal insolation, its effect on**
760 **tropical hydroclimate and the annual mean water isotopic composition.**

761 Solar radiation, or insolation, is the main source of energy reaching the earth, which gets
762 distributed between reflection (albedo), sensible heat (temperature), and latent heat upon
763 evaporation of water. At our site lake Nong Thale Prong at 8°N, the present-day annual
764 insolation curve exhibits two highs: one in April and one in August/September (Fig. S5),
765 when the sun's altitude is 90°C at noon. The annual movement of the ITCZ and the
766 Monsoon system behaves in an attenuated fashion (Fig. S6). From January onwards,
767 temperatures rise (Fig. S7) but precipitation remains low until May, because the ITCZ
768 remains south. Dry conditions with low cloud cover cause low albedo, resulting in highest
769 surface temperatures in April (Fig. S7). The ITCZ passes over quickly going northwards
770 during May and June, to merge with the Asian Summer Monsoon system during the NH
771 summer (Fig. S6). The Monsoon/ITCZ moves back towards the equator in NH autumn,
772 causing the strongest period of convective precipitation over the northern IPWP from
773 September-November (Figs. S6 and S7). During this time, much of the incoming radiation
774 is reflected by high convective clouds, or is used to generate latent heat, leading to
775 reduced surface temperatures (Fig. S7).

776

777 Between 6-4 ka BP, perihelium (the moment the earth is closest to the sun during its
778 elliptical orbit) occurred in September-October, causing 5% greater insolation in
779 September compared to today (Fig. S5). At the same time, insolation during early spring
780 was lower (Figs. S6 and S8). At the equator, a clear correlation exists between insolation
781 and rainfall amount, with at present lowest values in June and July (10) (Figs. S9 and
782 S10). Over the course of a precessional cycle, the shift in seasonal distribution of solar
783 energy can be as much as 15%, which must be causing a large effect on seasonality. At
784 and near the equator, the 'dry' season may even have shifted from NH summer to SH
785 summer (Fig. S9), and the wettest season more towards or away from the March and
786 September annual maximums, depending on the orbital phase. Because of this we did not

787 assign a wet season insolation curve to the Tangga Cave record at Sumatra (main Fig.
788 4). We reconstructed highest mean annual temperatures at our NTP site during the mid-
789 Holocene. Given the fact that total annual insolation hardly changes over the precessional
790 cycle, this must be caused by a shift to generally dryer conditions with clearer skies, most
791 likely during winter and spring. At the same time, our δD_{wax} record exhibits lowest values
792 during the mid-Holocene, indicating stronger convective activity during the autumn and/or
793 a greater relative contribution of isotopically more depleted precipitation in the (wettest)
794 months. Our data are thus consistent with the theory that the precessional cycle caused
795 greater seasonality in the mid Holocene, compared the low-seasonality period we
796 currently experience. At lake NTP, the water isotopic composition of precipitation is
797 primarily dependent on the convective activity as well as the isotopic composition of water
798 evaporated from the Indian Ocean ('source effect') (11). In the mid Holocene, stronger
799 insolation in NH summer and autumn, i.e. the wettest season insolation (WSI) for the SE
800 Asian Monsoon and the northern IPWP, will have caused warmer ocean surfaces and
801 subsequently greater evaporation and convective activity both in the northern Indian
802 Ocean (specifically the Bay of Bengal), as well as the South China sea.

803

804 At 20 kyr BP, the seasonal pattern of insolation is similar as today (Fig. S7), but over the
805 ensuing deglacial period (e.g., 14 ka BP) perihelion shifts towards NH spring. Being a
806 mirror case of the situation at 6 ka BP, this would cause higher convective activity in the
807 northern IPWP during spring with moisture sourced from the Pacific side. In NH autumn,
808 the lower insolation would have caused a weakened ITCZ convection. Different to today,
809 however, was the presence of Sundaland. Air masses coming from the northeast would
810 not have been able to pick up as much moisture as they can today over South China Sea.
811 Consequently, the greater NH spring insolation only could lead to more rainfall when
812 Sundaland became a large wetland, allowing more land surface evapotranspiration. Until
813 then, the annual sum of precipitation would have derived almost exclusively from the
814 autumn. After 14 ka BP, the perihelion moves towards NH summer, and insolation remains
815 high from spring through summer and into the autumn. After 12 ka BP, insolation becomes
816 ever more focused on the autumn (all autumn months go 'up', see Fig. S8), until 6 ka BP,
817 thus aligning ever more with the annual movement of the ITCZ and the period of strongest
818 convection. Over the last millenniums, perihelium has shifted from NH winter towards
819 spring.

820

821 The relative strength of insolation and related convective activity distributed over the year
822 will have had its effect on the annual weighted mean of δD of precipitation. Results for
823 nearby Phuket (11) indicate only a relatively small range in $\delta^{18}\text{O}$ through the year, from -
824 2‰ (i.e. $\delta D = -7‰$) in April to -8‰ ($\delta D = -55‰$) in November, with an annual weighted
825 average of -5.5‰ ($\delta D = -35‰$). The moment a shorter season is responsible for the
826 majority of the annual sum, i.e., when the perihelion aligns with the wettest months in
827 autumn, then the weighted mean annual isotope value will shift towards that season. This
828 is the likely situation in the mid Holocene around 6 ka BP where relatively heavy
829 (isotopically) spring precipitation will have contributed less, however the stronger
830 convective activity during the wet autumn season will likely have caused more depleted
831 wet season precipitation as well. Together this causes a bias towards lower mean annual
832 δD values at times of strong seasonality. This seasonal bias also means that there does

833 not need to be any close relation between total annual rainfall and the mean isotopic
834 composition. The seasonal bias on the mean annual isotopic composition can explain
835 many isotope records from the tropics, without a large need to infer changes in rainfall
836 amount, or changes in moisture source.

837

838 Lastly, we comment on the effect of the precessional cycle on advected moisture. In the
839 early Holocene, perihelion (i.e., highest insolation) occurred during the start of the Asian
840 summer monsoon, when the advected moisture in mainland SE Asia does not yet reach
841 very depleted values ($\delta^{18}\text{O} = -18\text{‰}$ (11)) In the mid-late Holocene, however, perihelion has
842 shifted to the autumn, at a time when the moisture reaching mainland SE Asia is already
843 much more depleted. The expected shift of the Monsoon strength towards the autumn will
844 thus also cause a shift in the mean isotope composition - even if at the local scale
845 insolation and therefore total monsoon strength has already decreased. The end result is
846 an attenuation of 'peak isotope', because of the source effect, and not because of the
847 amount effect. This effect can explain the temporal shift of 'peak isotope' away from the
848 time perihelium occurred during classical NH summer (JJA, between 10-8 ka BP) towards
849 later (8-6 ka BP) as observed in the Chinese speleothem records.

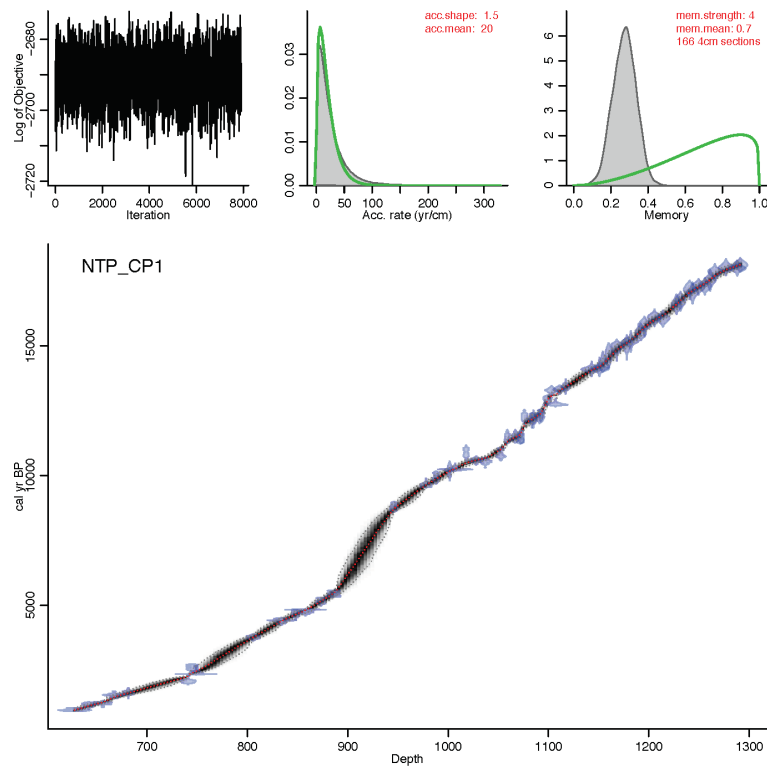
850

851

852

853 **Supplementary figures**

854

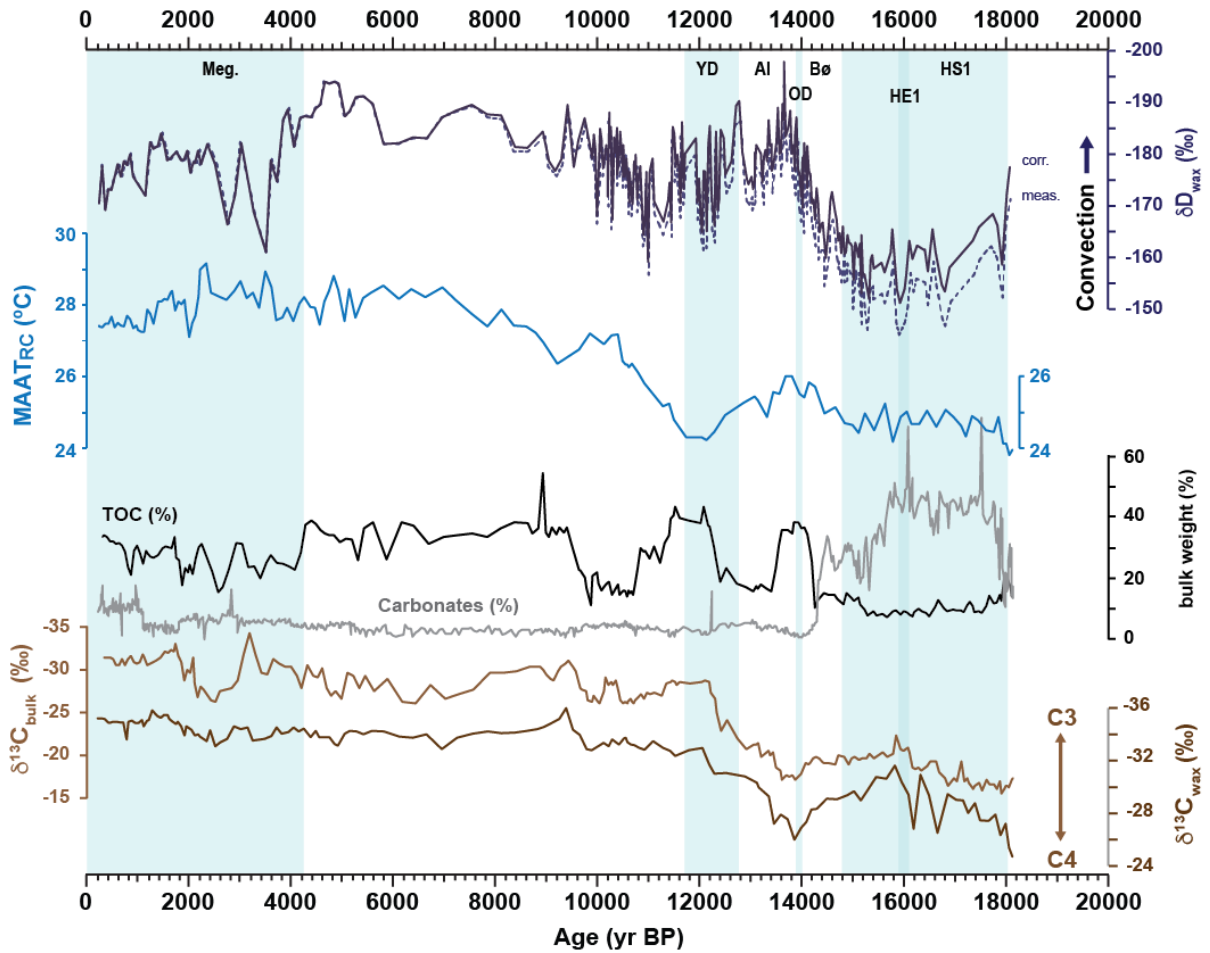


855

856

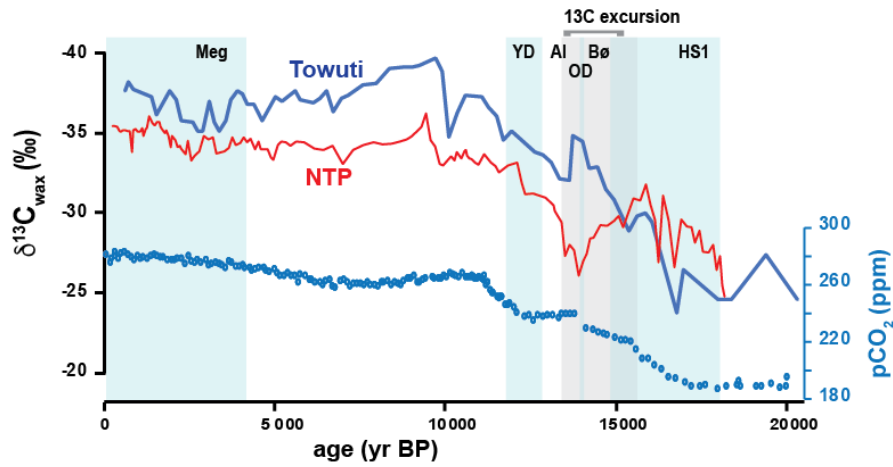
857 **Figure S1.** Age model of Lake Nong Thale Prong. Depth is expressed in meter below
858 lake level.

859



860
861
862
863

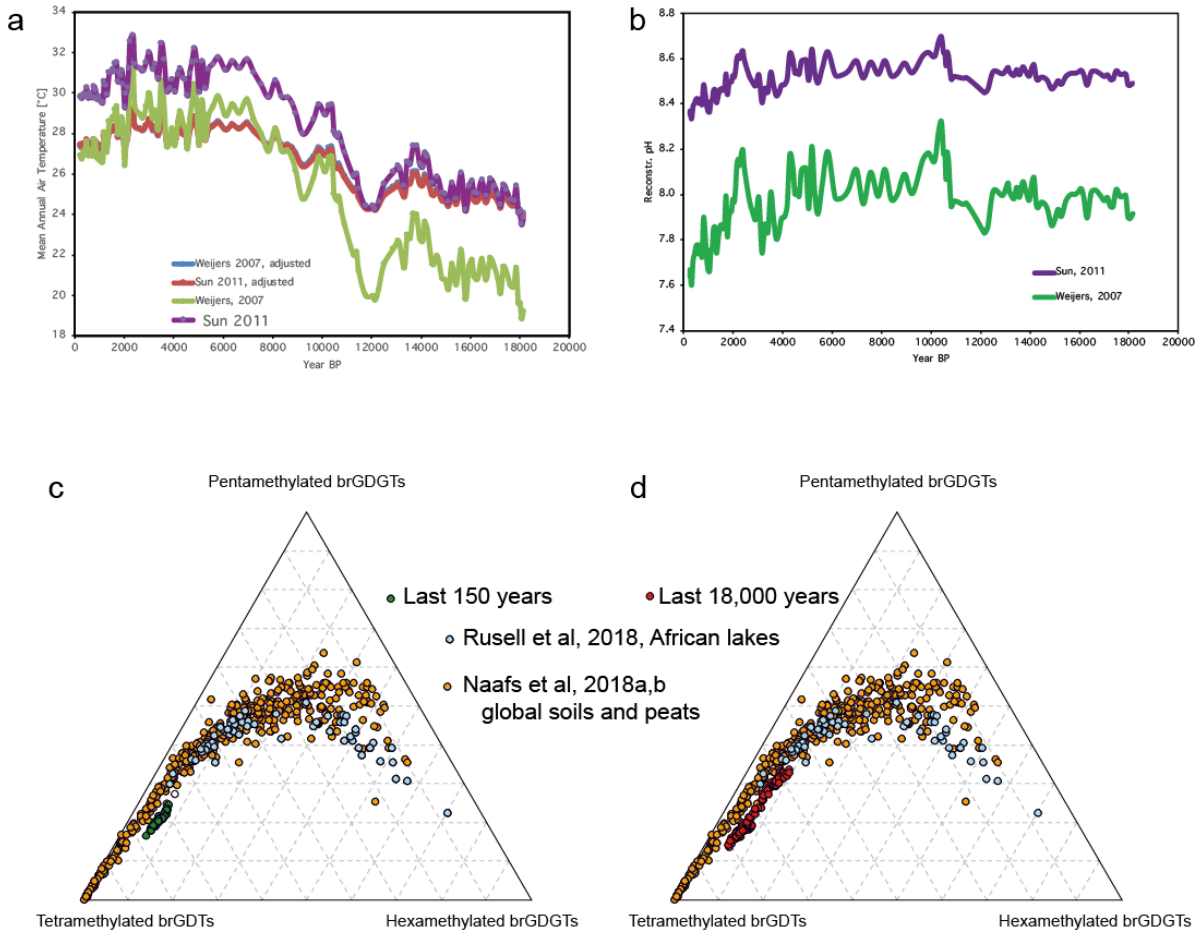
Figure S2. Proxy records of lake Nong Thale Prong, with elements of Fig. 3 in the main paper, extended with TOC content, bulk $\delta^{13}\text{C}$, and carbonate content based on loss-on-ignition.



864

865

866 **Figure S3.** Comparison of the $\delta^{13}\text{C}_{\text{wax}}$ records of lake NTP (this study) and lake Towuti
 867 (12) and atmospheric CO_2 levels (13).

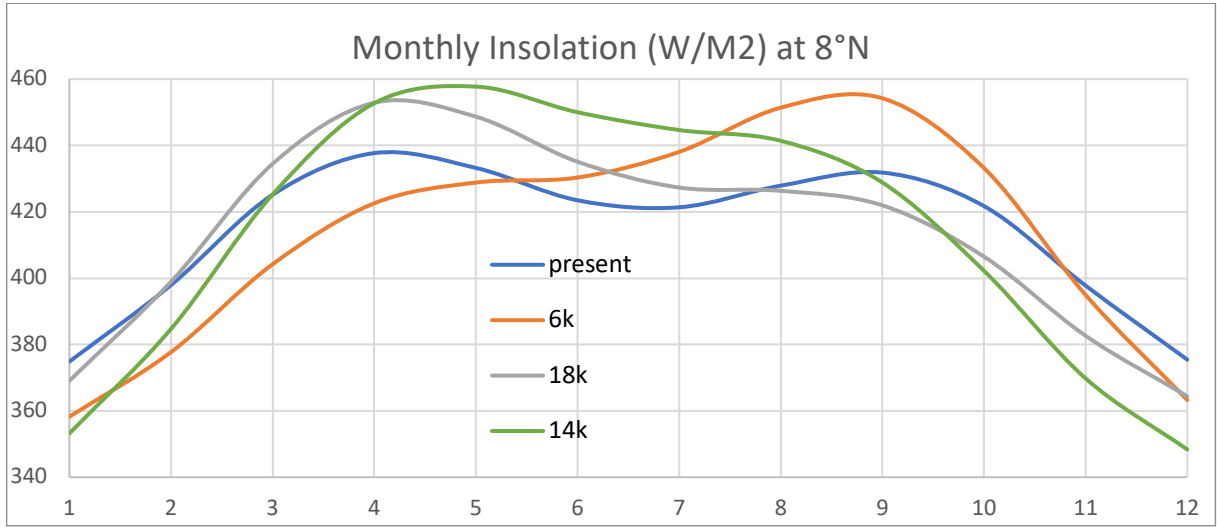


868

869

870 **Figure S4.** a) Reconstructed MAAT using the MBT/CBT ratios according to two
 871 calibrations (1)(8), and after local recalibration (adjusted) as described in the text. b)
 872 reconstructed pH using the CBT ratios (1)(8), c) Triplot of the relative abundance of
 873 tetra, penta- and hexamethylated GDGTs in the surface core (green); a pooled soil and
 874 peat (6)(14) (orange) and an African lake dataset (7)(light blue) are plotted for reference.
 875 d) the same as c, but for the long core NTP data (in red). The reference data set
 876 includes both the 5- and 6-methyl GDGTs, while the NTP dataset includes all isomers of
 877 the same *m/z*. Cindy de Jonge is acknowledged for making the triplots.

878



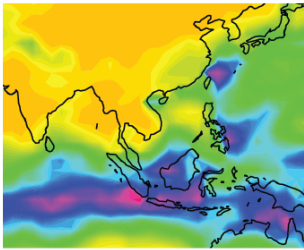
879

880

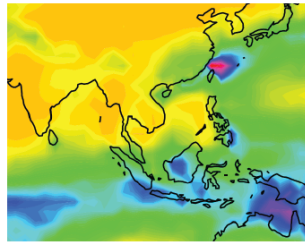
881 **Figure S5.** Annual insolation curves at 8°N over selected periods from the last 18,000
 882 years (15) clearly showing the two maximums in April and August/September. Months
 883 are in numbers.

884

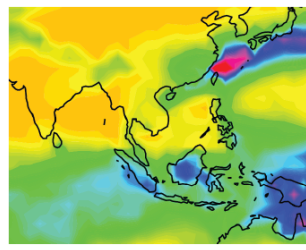
MSU/legates precipitation



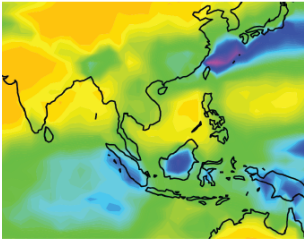
Jan



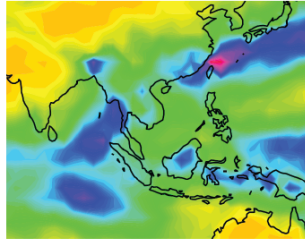
Feb



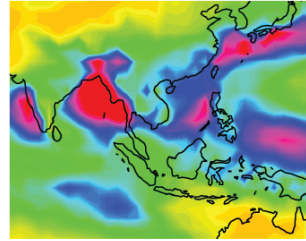
Mar



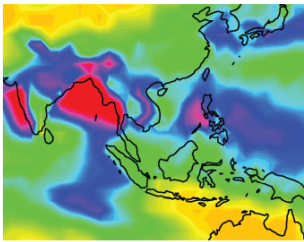
Apr



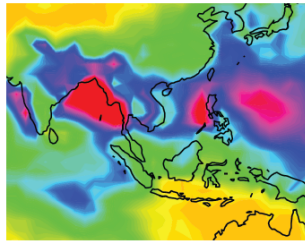
May



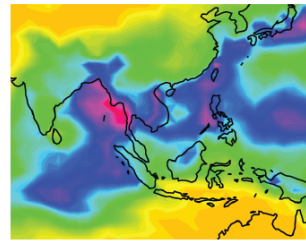
Jun



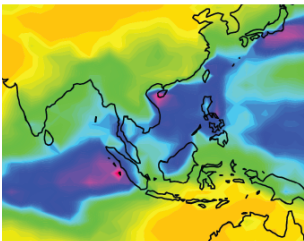
Jul



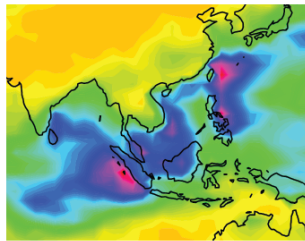
Aug



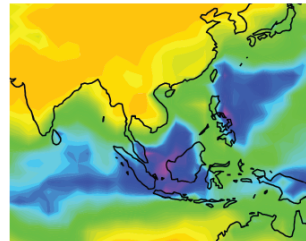
Sep



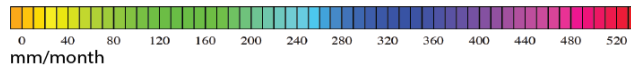
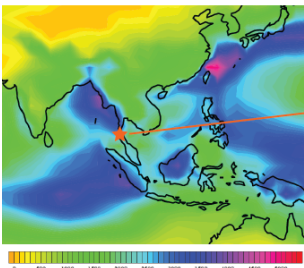
Oct



Nov



Dec



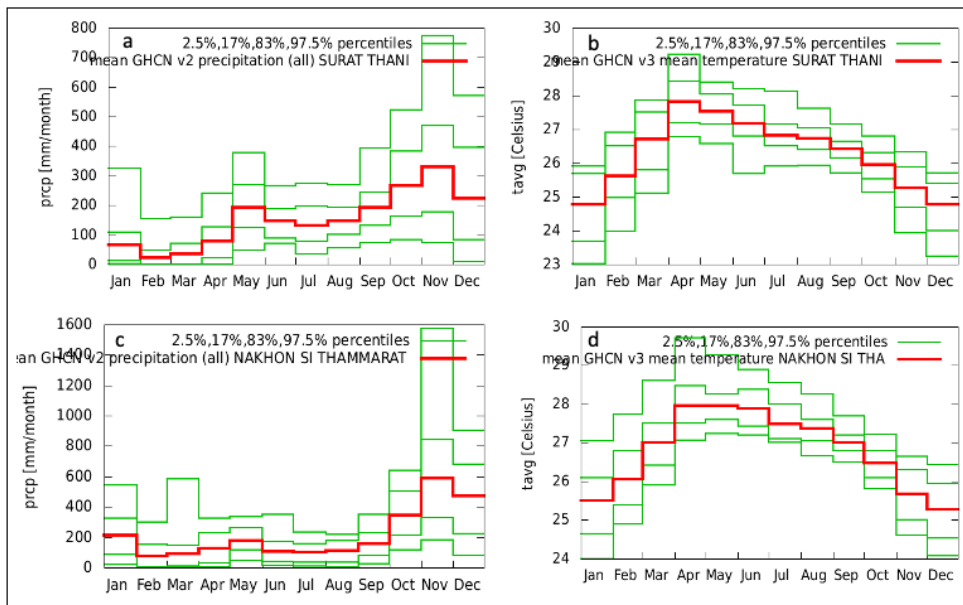
Lake Nong Thale Prong

Mean annual total (mm)

885

886

887 **Figure S6.** Monthly precipitation of the maritime continent and SE Asia. The wettest
888 months at Lake Nong Thale Prong are associated with the southward passing of the
889 ITCZ from September to November. Maps from
890 http://research.jisao.washington.edu/legates_msu/#analyses (Legates, D. R. and C. J.
891 Willmott, 1990. Mean seasonal and spatial variability in gauge-corrected, global
892 precipitation. *Int. J. Climatology*, 10, 111-127; Spencer, R. W., 1993: Global oceanic
893 precipitation from the MSU during 1979-91 and comparisons to other climatologies. *J.*
894 *Climate*, 6, 1301-1326)

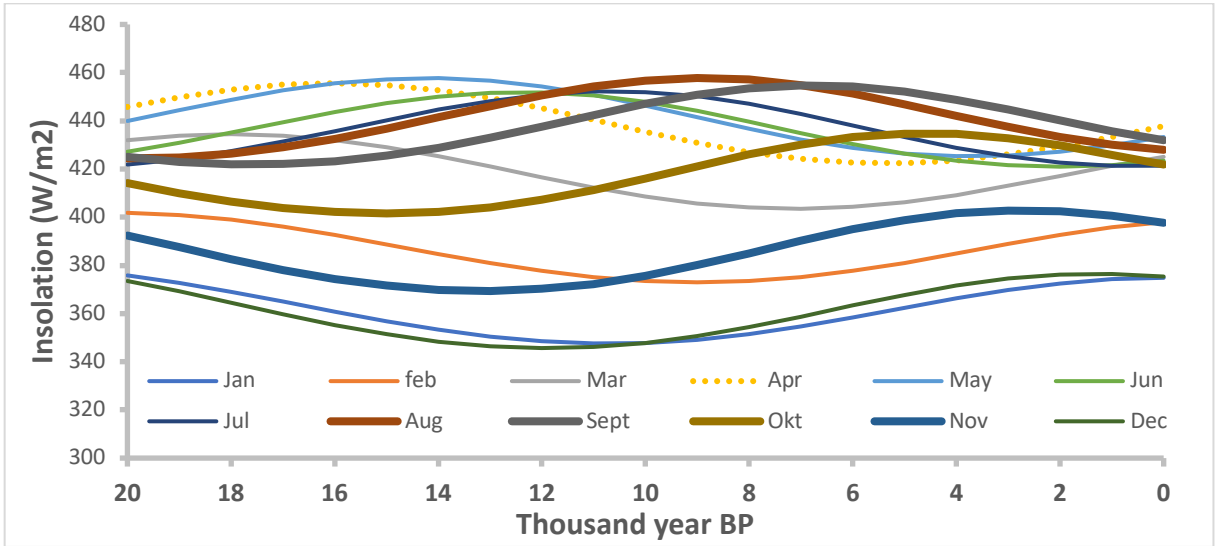


895

896 **Figure S7.** Monthly precipitation and mean temperature data from the two nearest
 897 weather stations to lake NTP, Surat Thani (9.12N, 99.35E) (a,b) and Nakhon Si
 898 Thammarat (c,d) (8.47N, 99.97E), obtained from the Global Historical Climatology
 899 Network (GHCN-Monthly) database Version 2.

900 The wettest period is September-November, running even into December (left panels);
 901 the warmest months are April-May. Reference: Thomas C. Peterson and Russell S.
 902 Vose (1997): Global Historical Climatology Network - Monthly (GHCN-M), Version 2.
 903 NOAA National Centers for Environmental Information. doi:10.7289/V5X34VDR
 904 [accessed 15 October 2020 using <http://climexp.knmi.nl>]

905



906

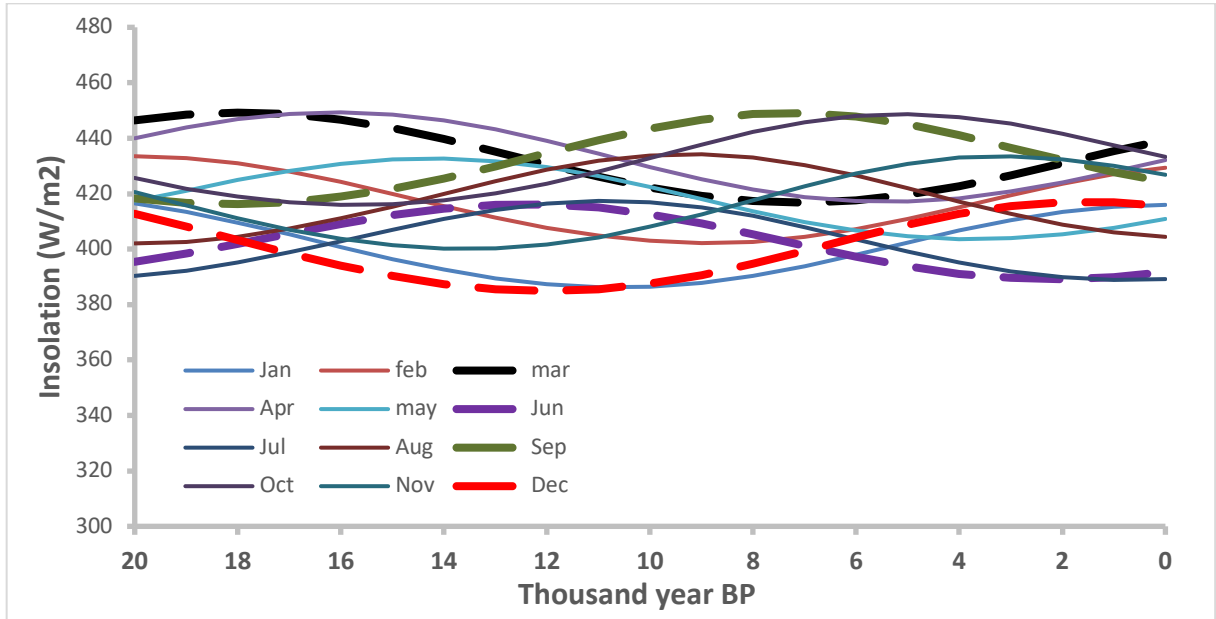
907 **Figure S8.** Mean monthly insolation (W/m²) over the last 20,000 years for 8°N (15),
 908 showing the waxing and waning of insolation energy over the precessional cycle for the
 909 various months. Insolation maximizes between 6-4 kyr BP for the wettest period SON
 910 (See Fig. S7). The insolation curves have the same shape for higher latitudes, but have
 911 different absolute values. The mainland SE Asian summer monsoon peaks in JAS, with
 912 highest insolation between 10-8 kyr BP and very low insolation at the present. Note that
 913 the age axis is reverse compared to proxy records.

914

915

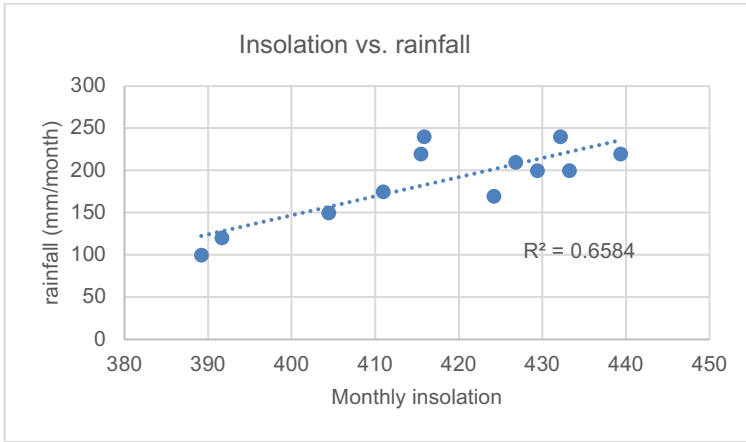
916

917



918
 919 **Figure S9.** As Figure S8 but for 0° (equator). Present-day June and July insolation are
 920 at their precessional low, and these months have correspondingly lowest rainfall
 921 amounts (see (10), while the months of December and January, with the same angle of
 922 the sun, have stronger insolation and greater rainfall (See Fig S10). Assuming a
 923 dominant influence of insolation on convective activity, the annual precipitation patterns
 924 likely changes over the course of the precessional cycle.

925



926

927 **Figure S10.** Cross plot of monthly rainfall against monthly insolation for 0° (equator),
928 showing a clear correlation between the two. Rainfall data taken from (10) and insolation
929 for the present day (0 ka BP) of Fig. S9.

930

931

932 **SI References**

- 933 1. J. W. H. Weijers, S. Schouten, J. C. van den Donker, E. C. Hopmans, J. S.
934 Sinninghe Damsté, Environmental controls on bacterial tetraether membrane lipid
935 distribution in soils. *Geochimica et Cosmochimica Acta* **71**, 703–713 (2007).
- 936 2. E. C. Hopmans, S. Schouten, J. S. Sinninghe Damsté, The effect of improved
937 chromatography on GDGT-based palaeoproxies. *Organic Geochemistry* **93**, 1–6
938 (2016).
- 939 3. J. E. Rattray, R. H. Smittenberg, Separation of Branched and Isoprenoid Glycerol
940 Dialkyl Glycerol Tetraether (GDGT) Isomers in Peat Soils and Marine Sediments
941 Using Reverse Phase Chromatography. *Front. Mar. Sci.* **7** (2020).
- 942 4. C. Zhu, *et al.*, Comprehensive glycerol ether lipid fingerprints through a novel
943 reversed phase liquid chromatography–mass spectrometry protocol. *Organic*
944 *Geochemistry* **65**, 53–62 (2013).
- 945 5. C. De Jonge, *et al.*, Occurrence and abundance of 6-methyl branched glycerol
946 dialkyl glycerol tetraethers in soils: Implications for palaeoclimate reconstruction.
947 *Geochimica et Cosmochimica Acta* **141**, 97–112 (2014).
- 948 6. B. D. A. Naafs, *et al.*, Introducing global peat-specific temperature and pH
949 calibrations based on brGDGT bacterial lipids. *Geochimica et Cosmochimica Acta*
950 **208**, 285–301 (2017).
- 951 7. J. M. Russell, E. C. Hopmans, S. E. Loomis, J. Liang, J. S. S. Damsté, Distributions
952 of 5- and 6-methyl branched glycerol dialkyl glycerol tetraethers (brGDGTs) in East
953 African lake sediment: Effects of temperature, pH, and new lacustrine
954 paleotemperature calibrations. *Organic Geochemistry* **117**, 56–69 (2018).
- 955 8. Q. Sun, *et al.*, Distributions and temperature dependence of branched glycerol
956 dialkyl glycerol tetraethers in recent lacustrine sediments from China and Nepal.
957 *Journal of Geophysical Research: Biogeosciences* **116** (2011).
- 958 9. I. Harris, P. D. Jones, T. J. Osborn, D. H. Lister, Updated high-resolution grids of
959 monthly climatic observations – the CRU TS3.10 Dataset. *International Journal of*
960 *Climatology* **34**, 623–642 (2014).
- 961 10. J. B. Wurtzel, *et al.*, Tropical Indo-Pacific hydroclimate response to North Atlantic
962 forcing during the last deglaciation as recorded by a speleothem from Sumatra,
963 Indonesia. *Earth and Planetary Science Letters* **492**, 264–278 (2018).
- 964 11. Z. Wei, *et al.*, Influences of large-scale convection and moisture source on monthly
965 precipitation isotope ratios observed in Thailand, Southeast Asia. *Earth and*
966 *Planetary Science Letters* **488**, 181–192 (2018).
- 967 12. J. M. Russell, *et al.*, Glacial forcing of central Indonesian hydroclimate since 60,000
968 y B.P. *Proceedings of the National Academy of Sciences* **111**, 5100–5105 (2014).
- 969 13. E. Monnin, EPICA Dome C high resolution carbon dioxide concentrations (2006)
970 <https://doi.org/10.1594/PANGAEA.472488> (January 6, 2021).
- 971 14. B. D. A. Naafs, A. V. Gallego-Sala, G. N. Inglis, R. D. Pancost, Refining the global
972 branched glycerol dialkyl glycerol tetraether (brGDGT) soil temperature calibration.
973 *Organic Geochemistry* **106**, 48–56 (2017).
- 974 15. J. Laskar, *et al.*, A long-term numerical solution for the insolation quantities of the
975 Earth. *A&A* **428**, 261–285 (2004).
- 976